Engineering Fracture Mechanics 289 (2023) 109413

Contents lists available at ScienceDirect

Engineering Fracture Mechanics

journal homepage: www.elsevier.com/locate/engfracmech

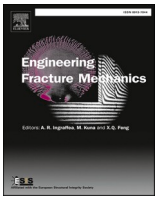

Numerical bond assessment of carbon-epoxy stepped-lap joints

Hugo C. Biscaia [a,b,*], Rui Micaelo [c], Pietro Cornetti [d], Raquel Almeida [a,b]

[a] UNIDEMI and Department of Mechanical and Industrial Engineering, NOVA School of Science and Technology, 2829-516 Caparica, Portugal
[b] Laboratório Associado de Sistemas Inteligentes, LASI, 4800-058 Guimarães, Portugal
[c] CERIS, Department of Civil Engineering, NOVA School of Science and Technology, Universidade NOVA de Lisboa, 2829-516 Caparica, Portugal
[d] Department of Structural, Geotechnical and Building Engineering, Politecnico di Torino, Corso Duca degli Abruzzi 24, 10129 Torino, Italy

ARTICLE INFO

Keywords:
Composite bonded joints
CFRP
Bond strength evaluation
Metallic structures
Numerical calculations

ABSTRACT

With the main purpose of obtaining lightweight and durable structures, bonding techniques have improved significantly in several industries. Depending on the type of structure, joining different components with different materials may require different joint geometries, which may perform better or worse. Still, only the bond performance of a very limited number of joint geometries is well known. A lack of knowledge, for instance, about the debonding process of one and two-step joints persists, especially for the latter. The present work intends to mitigate this gap by studying the debonding processes of one and two-step joints made with CFRP and aluminium adherends. To that end, implicit and explicit numerical methods (finite and distinct element methods, respectively), were applied to study different joint geometries and identify which one shows the best bond performance when subjected to a monotonic load consistent with pure fracture mode II. Based on the bond stresses obtained within the interface of the joints, the debonding propagations of the one and two-step joints are analyzed thoroughly. In the case of the one-step bonded joints, the results revealed that when the ratio between the axial stiffness of the adherends is $r = 1.0$ the load capacity of these joint configurations is maximized. With two-step joints, the load capacity is very sensitive to the relationship between the axial stiffness on the left (r_a) and right-hand side (r_b). Based on 162 different numerical simulations, the results also suggest that the load capacities of the two-step joint configurations can be maximized when the axial stiffness r_a and r_b of the joint are equal to 1/3 and 3.0, respectively.

1. Introduction

The use of bonded joints in different engineering applications such as aeronautic, civil, automotive or naval engineering is common. For instance, in the case of aeronautic engineering, airframe structures have several parts that are assembled to form the aircraft. In this process, various joints need to be designed to ensure that loads can be effectively transferred between components. To achieve this, mechanical fasteners and/or adhesives can be used. In the end, the aircraft should be as lightweight and high-strength as possible. Therefore, due to its high strength-to-weight ratio and good durability, the use of Carbon Fiber Reinforced Polymers (CFRP) in military and commercial aircraft has been growing. For instance, the Northrop Grumman B-2 stealth bomber is constructed almost entirely out of composite materials [1], whereas in commercial aircraft (Airbus A350 and Boeing 787), its use has only recently passed 50% of structural components (by weight) [2].

* Corresponding author.
E-mail address: hb@fct.unl.pt (H.C. Biscaia).

https://doi.org/10.1016/j.engfracmech.2023.109413
Received 22 February 2023; Received in revised form 22 May 2023; Accepted 7 June 2023
Available online 12 June 2023
0013-7944/© 2023 The Author(s). Published by Elsevier Ltd. This is an open access article under the CC BY-NC-ND license (http://creativecommons.org/licenses/by-nc-nd/4.0/).

The combination of CFRP composites with aluminium alloys allows us to preserve the original lightweight of aluminium structures. In the case of CFRP composite structures, the overlap of CFRP composites is common, which creates CFRP-to-CFRP joints. Furthermore, the use of composite materials in the repair of damaged reinforced concrete structures or in the repair of corroded steel structures has also grown, resulting in hybrid bonded joints of, e.g., CFRP and concrete [3–5] or steel [6–8], respectively. These joints are all challenging since CFRP composites by themselves may present complex failure mechanics. In addition, the use of mechanical fasteners along with the adhesives, the thickness of the adherends, the development of stress concentrations, the influence of temperature or the out-of-plane deformations on the edges of the joints are just some examples of factors that may contribute to the complexity of failure mechanics [9–11].

Adhesives, in their turn, also perform a key role in the integrity and final bond performance of the joint. There is an enormous variety of adhesives available in the market and the use of more ductile ones may increase the debonding loads of the joints when compared with the use of brittle adhesives [12–14]. Since the adhesive is usually the weakest element in the joint, the ideal situation is that the failure of the adherends occurs rather than the failure of the adhesive or the interfacial failure between the adherends and the adhesive. In this case, the integrity of the joint would be maximized but this is not a common failure mode and the cohesive rupture of the adhesive or its interfacial failure with one of the adherends are often both observed instead, e.g. [15–17]. The premature failure mode of the joint occurs when the strains of the adherends are much lower than their rupture strain. To delay or even prevent this premature failure mode, the geometry adopted for the joint is a very important aspect to consider. So, the rapid identification of the geometry of the joint associated with the best bond performance is only possible if the debonding process of each type of joint subjected to different conditions is well understood. Experimental-based research that considers several of these issues is very highly time-consuming. Therefore, the use of numerical strategies can be a helpful tool to compare feasible solutions in time. However, the modelling of CFRP-to-parent material joints requires previous knowledge of the local bond behaviour of the interface between materials, which is usually modelled on the Cohesive Zone Model (CZM). By relating the interfacial displacements with the interfacial stresses, the CZM tries to simulate the crack growth between materials allowing us to predict the debonding process of the joint.

Although different joint configurations have been used by different authors [18–23], the comprehensive analysis of the bond performance of only a few of them is described in the literature, e.g. [12,24–26]. Hart-Smith [18] proposed, in 1974, that the global strength of different bonded joints would be directly related to the configuration, thickness of the adherends or ductility of the adhesives. According to this author [18], the use of simple joints such as double-lap joints is better for thin adherends. However, beyond a certain thickness, simple joint configurations are not enough to load the structural members adequately and thicker adherends should be used instead. In this case, peeling stresses may occur and to avoid them, more complex joint geometries such as stepped-lap joints should be adopted. Despite this having often been repeated by other researchers since then [27–29], to the best of our knowledge, the existing studies, e.g. [30–32], do not confirm this influence of the joint strength and adhesive thickness with the joint configuration, either experimentally or numerically nor do they suggest a substantiated strategy. Thus, to get a deeper knowledge of the bond behaviour of more complex joint configurations, the debonding processes associated with each should be well understood first. To this end, a study of the bond stress distributions of different specimens with the same materials (adherends and adhesive), thicknesses, total bonded lengths, surface treatments, etc., subjected to a tensile mechanical load until failure is absolutely necessary. Moreover, the adoption of a sufficiently long bonded length is crucial for understanding the complete debonding process of the joints, both to gain a localised insight into the interpretation of the bond adherence between adherends (through the bond stress-slip relationship) and a global overview of the joints by analysing their load *versus* slip responses [19,20,33].

As mentioned before, despite the scarcity of studies on the comparison of different joint configurations, Kanani et al. [32] carried out an experimental campaign where scarf, stepped-lap, half-lap splice and single-lap joints were experimentally tested. In all, the same epoxy adhesive (Loctite EA 9497) and two types of adherends were used (aluminium and Polyphthalamide). The results achieved by the authors [32] allowed them to conclude that the scarf joint provided the best performance. However, it should be taken into account that the bonded lengths adopted by Kanani et al. [32], were all less than or equal to 50 mm, which are short bonded lengths and as a result induced them to conclude that not all the joint configurations benefited from the increase in bond length. It is worth mentioning that for the scarf joint, the interface is under a mixed mode I + II loading where the presence of peeling stresses reduces the magnitude of the bond stresses developed in the joint, as described in the literature [34], leading, therefore, to a reduction of the load capacity of the joints, which seems to contradict the conclusions reached by Kanani et al. [32].

Double-strap joints under a pull-pull condition are also commonly used to study the bond performance of CFRP composites externally bonded to steel, e.g. [10,26,35,36]. Taking advantage of its symmetry, the development of peeling stresses in the overlapped length is mitigated, which allows researchers to define the mode II bond behaviour between adherends (usually denoted as bond-slip relationship). Based on this type of joint, Fawzia et al. [35] concluded that the bond-slip relationship is influenced by the thickness of the adhesive, i.e. the increase of the thickness of the adhesive increases the slips of the CFRP-to-steel joints. The ratio (r) between the axial stiffnesses of the adherends is another important parameter that influences the load capacity of double-strap joints. For instance, the load capacity of a double-strap joint is maximized when $r = 1$, but in the case of a double-strap joint with a very low r value, the debonding process becomes quite similar to that which is observed in single or double-lap joints under a pull–push condition. Since in the double-strap joints both adherends are pulled out, the bond stresses within the interface are located close to both pulled ends, whereas in the single or double-lap joints the bond stresses mainly develop close to the pulled end region of the joint [26].

Since peeling stresses are more damaging to the integrity of the joints, the use of a multi-stepped configuration rather than a one-stepped joint configuration is intended to reduce the effect they have on the debonding load of the joint. So, Durmuş and Akpinar [31] have carried out experimental and numerical studies on the mechanical properties of three different (AA2024-T3) aluminium-to-aluminium joint configurations: single lap joint, one-step lap joint and three-step lap joint with five different step lengths. In all, the same bonding area was kept and the two adherends were bonded by the structural adhesive DP460. The results showed that the

three-step joints were able to carry more load than any other joint. Despite the load capacities of the one-step joints being 9.5% higher than those of the single-lap joints, the authors [31] also found that by simply increasing the outer steps of the three-step lap joints by 8 mm each, the load capacities of the three-step lap joints could duplicate that of the single lap joints.

Based on the literature review, it can be asseverated that while the debonding processes of single and double overlapped joints are well known and described in the literature [12,19,20,37–41], the same cannot be said, for instance, for one or two-step (or even for three-step) joints. Consequently, further studies should be carried out to clarify all these aspects.

2. Objectives and scope

The current work aims to mitigate the current knowledge gap in the literature on the stepped-lap bonded joints by numerically analysing a series of different bonded joints with one and two-step configurations. To ensure the robustness of the present study, the Finite Element Method (FEM) and the Distinct Element Method (DEM), which follow different formulations (implicit and explicit methods, respectively) were used to model and analyse a series of different stepped-lap joints with different geometries and materials. To that end, the influence of the following two parameters on the debonding process of these joints is evaluated: (a) the elastic modulus of the adherends; and (b) the ratio between the axial stiffnesses of the adherends defined as:

$$r = \frac{E_2 \cdot t_2}{E_1 \cdot t_1} \tag{1}$$

where E_1 and E_2 are the elastic modulus of the inner and outer materials of the bonded joint, respectively; and t_1 and t_2 are the thickness of the inner and outer materials of the bonded joint, respectively. For the analysis of the influence of the elastic modulus of the adherends, two different materials are used: CFRP and aluminium. With CFRP being considered the essential material, CFRP-to-aluminium and CFRP-to-CFRP bonded joints were studied in this work. The value of the ratio between the axial stiffness of the adherends defined in (1) has a relevant influence on the debonding process of double-strap bonded joints [26]. To analyse if the same occurs in one-step and two-step bonded joints, a wide range of debonding processes with five different r values are considered (r = 0.19, 0.78, 1.00, 1.28 and 5.14). Based on the different debonding processes identified for the two-step bonded joints, an optimized geometry able to maximize the load capacity of these joints is investigated thoroughly.

3. Definition of the stepped bonded joints

3.1. Materials

To conceive the bonded joints, a CFRP composite and an aluminium alloy were considered in this study. Unidirectional CFRP composites usually show a linear stress–strain relationship until failure. Hence, an elastic modulus of E_f = 180 GPa with a strain rupture of $\varepsilon_{f,r}$ = 1.03% was used for this composite material. Although aluminium alloys typically have a fully nonlinear constitutive behaviour until failure [42–45], as a simplification, a bilinear model with hardening for aluminium was adopted. To avoid the yielding of the aluminium and subsequent influence on the debonding processes of the bonded joints, the 7050 aluminium alloy with an elastic modulus of E_a = 70.0 GPa, yielding strain of $\varepsilon_{a,y}$ = 0.65%, and rupture stress of $f_{a,r}$ = 515 MPa was selected. Fig. 1a shows the constitutive behaviours of the CFRP composite and the 7050 aluminium alloy considered in this work.

3.2. Local bond behaviour

The interfaces between adherends are modelled by a Cohesive Zone Model (CZM) with a triangular shape (bilinear law). The local bond behaviour is, therefore, modelled through a bond-slip relationship which allows us to correlate the interfacial slip (s) within the interface with the bond stress (τ_1) developed at each point of the bonded length of the joint. Although several bond-slip relationships

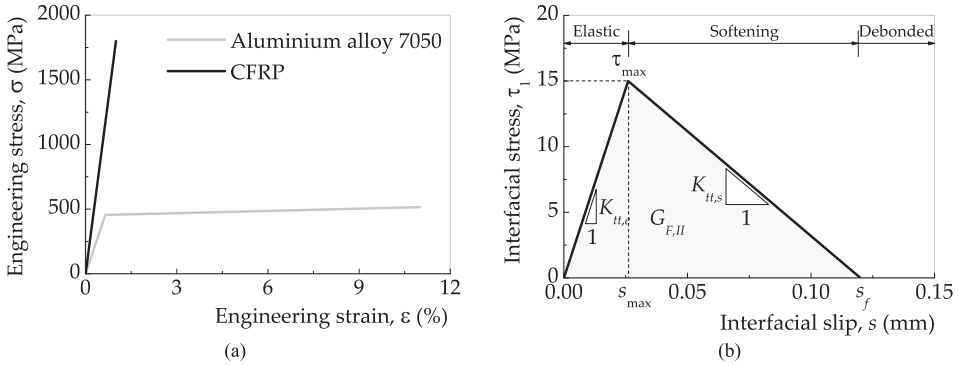

Fig. 1. Definition of mechanical properties of the materials: (a) CFRP and aluminium; and (b) interface CFRP-to-aluminium (or CFRP).

can be found in the literature, e.g. [12,19,33,45–49], the bilinear one is commonly accepted for the modelling of the local bond behaviour of bonded joints with elastic adherends [48], whereas exponential or trilinear bond-slip relationships are often recommended for nonlinear adherends such as concrete [33,50] or wood [51], respectively. The bilinear bond-slip model is defined by three different stages, as shown in Fig. 1b. The first stage is the Elastic (E) stage, which is defined by an elastic stiffness ($K_{tt,e}$) and is limited by a maximum bond stress (τ_{max}) value and its corresponding interfacial slip (s_{max}). The next stage, the Softening (S) stage, is characterized by a linear reduction of τ_{max} with the interfacial slip. The Softening stage ends when the final interfacial slip (s_f) is reached. Beyond this interfacial slip s_f, the materials physically detach from each other and, therefore, the bond stress transfer between them is cancelled.

To limit the number of variants in this study, the same bilinear bond-slip relationship was used in all the numerical models in which the maximum bond stress was set equal to 15.0 MPa, the elastic stiffness ($K_{tt,e}$) was set equal to 5.769×10^5 MN/m^3 (corresponding to a $s_{max} = 0.026$ mm) and a final interfacial slip of $s_f = 0.12$ mm (see Fig. 1b). Consequently, the value of the Mode II fracture energy, calculated from the area limited by the bond-slip relationship, is always $G_{F,II} = 0.900$ N/mm. Although summarized, further details about the CZM model used in this work will be given in Subsection 4.1.

3.3. Geometry of the specimens

To cover a large range of multi-stepped configurations and to evaluate the bond capacities and debonding processes of each bonded joint, a total of 83 models were initially idealized and covered two different configurations. The first group consisted of joints where the materials were joined through a one-step configuration (see Fig. 2a), whereas the joining of both materials of the other group followed a two-step configuration as illustrated in Fig. 2b. In this study, material 1 is on the left-hand side of the joint and material 2 is on the right. The ratio between the axial stiffnesses of the materials (r) influences the debonding process of the joints [26], and since this value changes in the two-step bonded joints, the following two axial stiffnesses were defined:

$$r_a = \frac{E_2 \cdot t_{a2}}{E_1 \cdot t_{a1}} \tag{2}$$

and

$$r_b = \frac{E_2 \cdot t_{b2}}{E_1 \cdot t_{b1}} \tag{3}$$

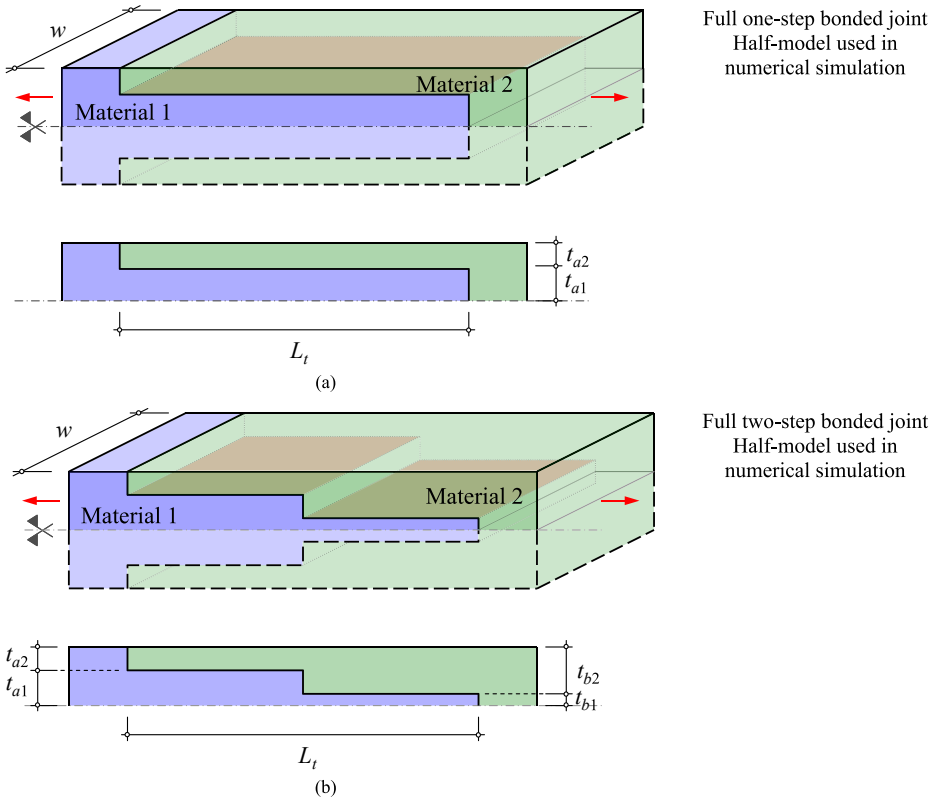

Fig. 2. Illustration of the: (a) one-step bonded joint; and (b) two-step bonded joint.

where E_1 and E_2 are the elastic moduli of material 1 and 2, respectively; t_{a1} and t_{a2} are the thicknesses of material 1 and material 2 on the left-hand side of the joint, respectively; and t_{b1} and t_{b2} are the thicknesses of material 1 and material 2 on the right-hand side of the joint, respectively.

Therefore, the axial stiffness r_a in Eq. (2) stands for the axial stiffness ratio on one-step bonded joints and the left-hand side of the two-step bonded joints whilst r_b in Eq. (3) corresponds to the axial stiffness ratio on the right of the same bonded joint. To cover a wide range of different situations, three different axial stiffness ratios were selected, with r_a and r_b equal to 0.19, 0.78, and 1.00. For instance, considering Fig. 2a and assuming $r_a = 0.19$, means that the axial stiffness of material 1 is almost 5 times the axial stiffness of material 2. In such a case, since r is quite low, it is expected that the debonding process of the one-step joint configuration may develop a softening stage only on its left, and therefore, it is from this side that the joint initiates its debonding [26]. With an axial stiffness closer to 1 (for instance, with $r_a = 0.78$) it is expected that the debonding process may develop a softening stage at both ends of the joint. However, the debonding commences always from left to right [26]. In the third situation, i.e. when $r_a = 1.00$, the debonding process is symmetric and the separation of materials is carried out symmetrically also. It should be noted also that when the axial stiffness is higher than 1, the debonding process is similar to the cases of $r_a < 1$ but the debonding process commences on the other side of the joint, i.e. on the right-hand side of the joint and spreads left.

The first specimens adopted in this study are listed in Table 1. Two series were considered, series C/C and C/A. The first assumes that the adherends are the same, i.e. CFRP composite. In this case, only the thickness of the CFRP influences the axial stiffness ratio. In the other case (C/A), the adherends are the CFRP composite and aluminium, and the axial stiffness is affected by the elastic modulus of the materials as well as the thickness of both materials. To ensure that the configuration shown in Fig. 2 is preserved, i.e. the two-step joints where the thickness of material 1 increased towards the end were not considered, a total of 40 possible combinations were identified. So, to facilitate the identification of each specimen and their results as well as the subsequent discussions, the ID of the specimens was defined as follows: “C/X”_“YS”_“ra”_“rb”_“Lt”, where “X” corresponds to the second adherend, where “C” refers to the

Table 1
Identification of the numerical models.

ID of the numerical model	Elastic modulus (GPa)	Thickness (mm)	Axial stiffness ratios (-)	Joint configuration type	Total bonded length L_t (mm)
	Mat. 1 | Mat. 2	t_{a1} & t_{a2} | t_{b1} & t_{b2}	r_a | r_b		
C/C_OS_r0.19_L75	180 | 180	4.69 & 0.91 | -	0.19 | -	One-step	75
C/C_OS_r0.19_L150					150
C/C_OS_r0.78_L75		3.15 & 2.45 | -	0.78 | -		75
C/C_OS_r0.78_L150					150
C/C_OS_r1.00_L75		2.80 & 2.80 | -	1.00 | -		75
C/C_OS_r1.00_L150					150
C/C_OS_r1.29_L75		2.45 & 3.15 | -	1.29 | -		75
C/C_OS_r1.29_L150					150
C/C_OS_r5.14_L75		0.91 & 4.69 | -	5.14 | -		75
C/C_OS_r5.14_L150					150
C/A_OS_r0.19_L75	180 | 70	3.73 & 1.87 | -	0.19 | -		75
C/A_OS_r0.19_L150					150
C/A_OS_r0.78_L75		1.86 & 3.74 | -	0.78 | -		75
C/A_OS_r0.78_L150					150
C/A_OS_r1.00_L75		1.57 & 4.03 | -	1.00 | -		75
C/A_OS_r1.00_L150					150
C/A_OS_r1.29_L75		3.74 & 1.86 | -	1.29 | -		75
C/A_OS_r1.29_L150					150
C/A_OS_r5.14_L75		1.87 & 3.73 | -	5.14 | -		75
C/A_OS_r5.14_L150					150
C/C_TS_r0.19/r0.78_L150	180 | 180	4.69 & 0.91 | 3.15 & 2.45	0.19 | 0.78	Two-step	150
C/C_TS_r0.19/r1.00_L150		4.69 & 0.91 | 2.80 & 2.80	0.19 | 1.00		
C/C_TS_r0.19/r1.29_L150		4.69 & 0.91 | 2.45 & 3.15	0.19 | 1.29		
C/C_TS_r0.19/r5.14_L150		4.69 & 0.91 | 0.91 & 4.69	0.19 | 5.14		
C/C_TS_r0.78/r1.00_L150		3.15 & 2.45 | 2.80 & 2.80	0.78 | 1.00		
C/C_TS_r0.78/r1.29_L150		3.15 & 2.45 | 2.45 & 3.15	0.78 | 1.29		
C/C_TS_r0.78/r5.14_L150		3.15 & 2.45 | 0.91 & 4.69	0.78 | 5.14		
C/C_TS_r1.00/r1.29_L150		2.80 & 2.80 | 2.45 & 3.15	1.00 | 1.29		
C/C_TS_r1.00/r5.14_L150		2.80 & 2.80 | 0.91 & 4.69	1.00 | 5.14		
C/C_TS_r1.29/r5.14_L150		2.45 & 3.15 | 0.91 & 4.69	1.29 | 5.14		
C/A_TS_r0.19/r0.78_L150	180 | 70	3.73 & 1.87 | 1.86 & 3.74	0.19 | 0.78		
C/A_TS_r0.19/r1.00_L150		3.73 & 1.87 | 1.57 & 4.03	0.19 | 1.00		
C/A_TS_r0.19/r1.29_L150		3.73 & 1.87 | 1.30 & 4.30	0.19 | 1.29		
C/A_TS_r0.19/r5.14_L150		3.73 & 1.87 | 0.39 & 5.21	0.19 | 5.14		
C/A_TS_r0.78/r1.00_L150		1.86 & 3.74 | 1.57 & 4.03	0.78 | 1.00		
C/A_TS_r0.78/r1.29_L150		1.86 & 3.74 | 1.30 & 4.30	0.78 | 1.29		
C/A_TS_r0.78/r5.14_L150		1.86 & 3.74 | 0.39 & 5.21	0.78 | 5.14		
C/A_TS_r1.00/r1.29_L150		1.57 & 4.03 | 1.30 & 4.30	1.00 | 1.29		
C/A_TS_r1.00/r5.14_L150		1.57 & 4.03 | 0.39 & 5.21	1.00 | 5.14		
C/A_TS_r1.29/r5.14_L150		1.30 & 4.30 | 0.39 & 5.21	1.29 | 5.14		

CFRP composite, while "A" corresponds to the aluminium; "YS" defines the configuration type of the joint (OS stands for One-Step and TS stands for Two-Step); "ra" or "rb" defines the axial stiffness ratio adopted in each step of the joint and, for obvious reasons, in the case of the one-step joint configuration only one value of r is shown; and "Lt" indicates the total length adopted for the bonded joint. In the case of the two-step joints, both steps had the same bonded length, i.e. for a total bonded length of 150 mm, each step had a bonded length of 75 mm. For instance, model C/A_TS_r0.78_r1.00_L150 corresponds to the numerical simulation of the adhesively bonded joint between the CFRP and aluminium where the first and second steps of the joint have an axial stiffness of 0.78 and 1.00, respectively, and a total length of 150 mm.

4. Numerical analysis

4.1. The finite element method (FEM)

All the models assume that the bond stresses have a uniform distribution alongside the width of the bonded joint. Therefore, and for the sake of the simplicity, the 2D version of the commercial software ATENA [52] with was used. Moreover, reducing the number of finite elements also reduces the number of nonlinear equations to be solved through the Newton-Raphson Method, which saves time during the solving of the numerical simulations. This software [52] also proved [26,46,53–55] to be effective enough in the prediction of the bond behaviour of hybrid joints with elastic adherends subjected to mechanical and thermal loadings.

Based on previous studies by the authors [48,55], the present numerical models consisted of two macro-elements with a quadrilateral mesh of 0.5 mm in which the shape of the elements can be smoothed in some parts of the models. Due to symmetry, only one-half of the joint (the upper part) was modelled as shown in Fig. 2. The CFRP and the aluminium were simulated through the "3D Bilinear Steel Von Mises" material available in the software [52], which assumes a plain strain idealization. The interfaces were all modelled as they had no thickness. Depending on the direction of the interface, i.e. parallel or perpendicular to the application of the loads, the interface was modelled differently. Thus, no contact was assumed within the interfaces of the joints perpendicularly positioned with the loads (see Fig. 3). The interfaces parallel to the loads were modelled through a CZM based on the Mohr-Coulomb failure criterion. Briefly, this CZM allows the coupling of the three fracture modes, i.e. Modes I, II, and III. The first fracture mode is related to the opening mode of the crack between adherends and it is responsible for the appearance of peeling stresses (σ) that develop perpendicularly to the bonded surface. The other two fracture modes, Modes II and III, are, respectively, the sliding and the tearing modes, and both are responsible for the development of in-plane and anti-plane stresses (τ_1 and τ_2, respectively), i.e. stresses developed in the same plane of the bonded area of the joint perpendicular to each other. Moreover, under the influence of these fracture modes, the behaviour of the joints in a three-dimensional problem is given by a constitutive relation defined as:

$$\begin{Bmatrix} \sigma_n \\ \tau_1 \\ \tau_2 \end{Bmatrix} = \begin{bmatrix} K_{nn} & 0 & 0 \\ 0 & K_{tt} & 0 \\ 0 & 0 & K_{tt} \end{bmatrix} \cdot \begin{Bmatrix} u \\ s \\ v \end{Bmatrix} \tag{4}$$

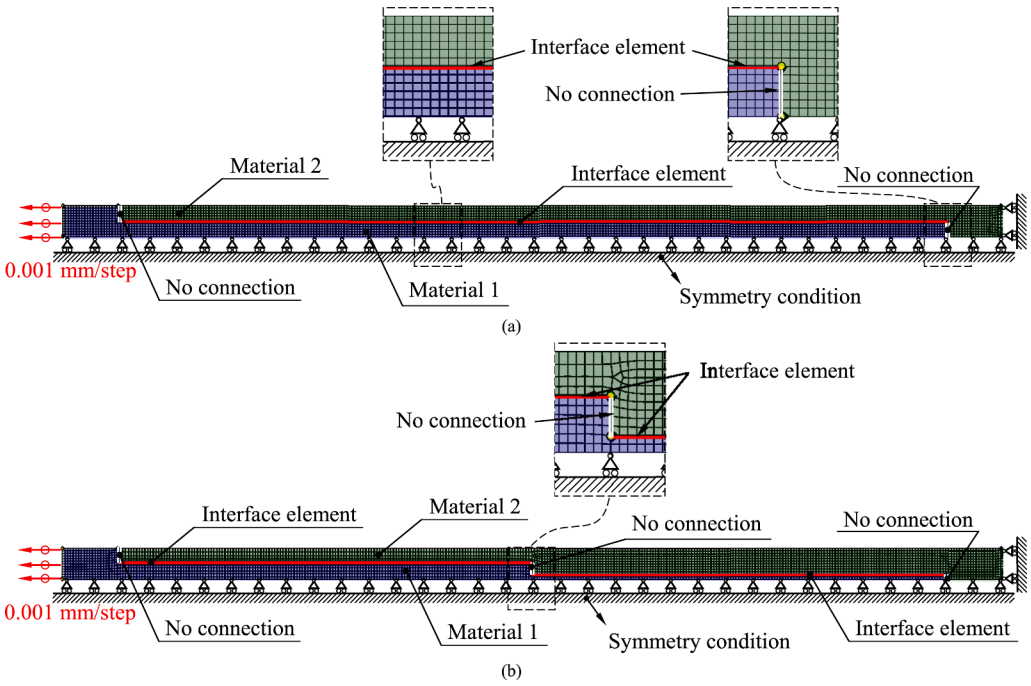

Fig. 3. Example of the finite element models of specimens: (a) C/C_OS_r1.00_L150; and (b) C/C_TS_r0.78/r5.14_L150.

where K_{nn} and K_{tt} are the normal and tangential stiffnesses of the interface, respectively; and u, s, and v are the interfacial slips according to Modes I, II, and III, respectively. Naturally, once a 2D analysis is carried out, the last line of Eq. (4) is eliminated. Moreover, the maximum value reached by the bond stress τ_1 in Eq. (4) corresponds to the value of cohesion (c) in the Mohr-Coulomb criterion [34,53]. The friction angle (ϕ) is another important parameter that is mainly responsible for the coupling of Modes I and II. Since in the present case the expected failure mode will be consistent with Mode II, to avoid interferences between modes, the friction angle should be set equal to zero [49,54]. In addition, the values of K_{nn} and σ_n in Eq. (4) were set very high (2×10^{12} MN/mm^3 and 100 MPa, respectively), to avoid any failure under fracture Mode I. No softening was used in this normal direction. To obtain more details about this CZM, the readers are advised to read other published works carried out by the authors [34,48,53,55].

The loads were simulated by a regular displacement increment of 0.001 mm/step until the failure is predicted. The displacements in the adherends near the interfaces of the joints were monitored every 5 mm, and since the interfacial slips (s) are the relative displacements between them, the following expression was used

$$s = S_2 - S_1 \tag{5}$$

where S_1 and S_2 are the displacements in adherends 1 and 2, respectively.

Fig. 3 shows typical finite element models for the one-step (in Fig. 3a) and two-step (in Fig. 3b) bonded joints. In Fig. 3a, specimen C/C_OS_r1.00_L150 is illustrated, whereas in Fig. 3b shows the two-step bonded joint of specimen C/C_TS_r0.78/r5.14_L150.

4.2. The distinct element method (DEM)

The Distinct Element Method (DEM) is an alternative numerical approach to the FEM and it was implemented also for the simulation of the selected carbon-epoxy stepped joints described before. The DEM is a micromechanical numerical method that has already proven to be suitable for the study of engineering problems, such as geotechnical, building materials, mining or pharmaceutical problems [56–59]. In this micromechanical method, the material is discretized by an assembly of rigid particles whose individual displacement and rotation are a consequence of the set of forces acting on it. The particle's motion is determined by Newton's second law. Each particle can interact with other particles found in the vicinity through soft contact points, which means that when particles are overlapped, a compressive force is generated. The contact stiffnesses in normal and shear directions are defined by the contact models assigned to each contact. The DEM is available with two (2D) and three-dimensional (3D) formulations but since it is a numerical method with very high computational demands, the 2D DEM version is often used to speed up the calculations when the problem can be simplified to a single plane such as the ones being studied here.

Since it has been effectively used before to characterize the mechanical behaviour of bonded joints made of different adherend

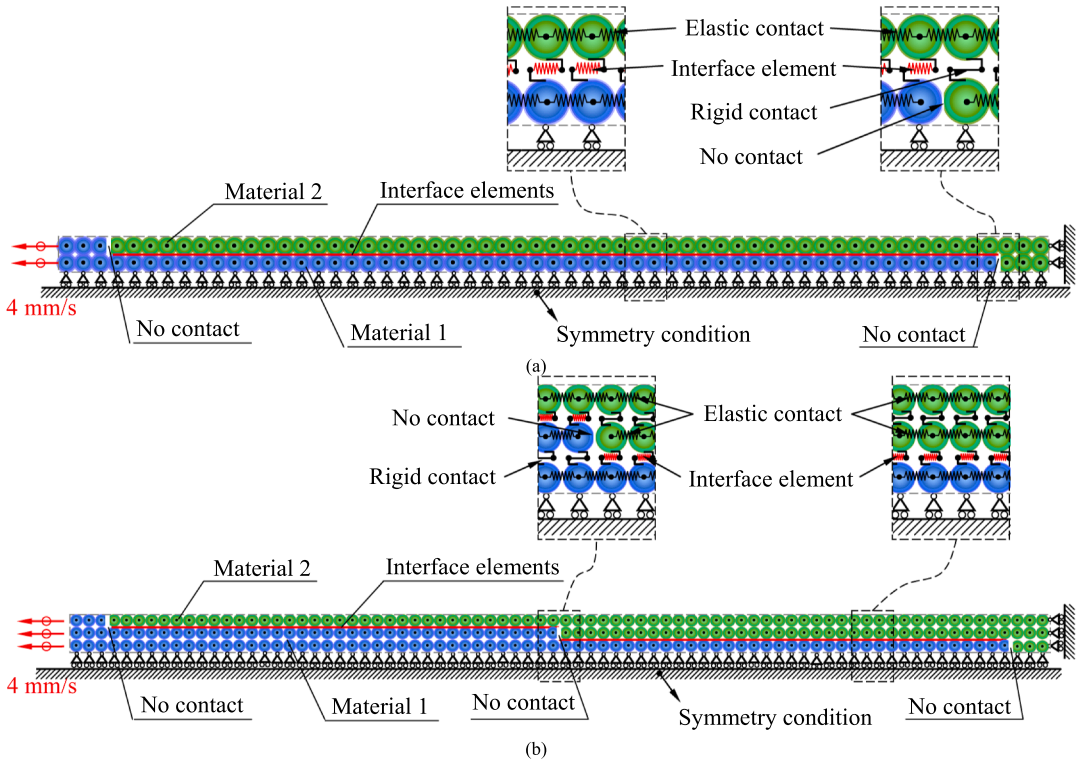

Fig. 4. Example of the distinct element models of specimens: (a) C/C_OS_r1.00_L150; and (b) C/C_TS_r0.78/r5.14_L150.

materials such as CFRP-to-concrete [60] or CFRP-to-steel [61], the 2D DEM version described in the literature [57,62] was used in this study as well. Like the models carried out in the FEM, one-half of the stepped joints were also considered in the DEM. The bonded joints were discretized in equally sized circular particles (radius of 0.5 mm) in two and three layers for one and two-step joints, respectively, as illustrated in Fig. 4. In the out-of-plane direction, the circular particles have constant width (1 m for simplicity), which means that the modelled assembly is a collection of cylinders vertically aligned on a single plane. The effect of the material thickness in both one and two-stepped configurations was incorporated through the contact stiffness.

At each contact point between particles, an incremental linear formulation (force–displacement law) is used to define the normal (ΔF^n) and shear (ΔF^s) force increments in time ($t + \Delta t$) as follows:

$$\Delta F^n_{t+\Delta t} = -k^n \cdot \Delta U_{t+\Delta t} \tag{6}$$

$$\Delta F^s_{t+\Delta t} = -k^s \cdot \Delta S_{t+\Delta t} \tag{7}$$

where ΔU and ΔS are the normal and shear contact displacements, and k^n and k^s are, respectively, the normal and shear contact stiffnesses defined according to:

$$k^n = \frac{E \cdot w \cdot t}{2R} \tag{8}$$

$$k^s = \begin{cases} \dfrac{K_{tt} \cdot w}{2R} & \text{if } s \leqslant s_{\max} \\ -\dfrac{K_{tt} \cdot w}{2R} & \text{if } s > s_{\max} \end{cases} \tag{9}$$

Table 2
Load capacities of the stepped bonded joints.

Numerical model	FEM (kN)	DEM (kN)	$F^{(FEM)}_{\max}/F^{(DEM)}_{\max}$	Absolute deviation (kN)
C/C_OS_r0.19_L75	29.42	29.35	1.002	0.07
C/C_OS_r0.19_L150	29.80	29.87	0.998	0.07
C/C_OS_r0.78_L75	48.13	48.02	1.002	0.09
C/C_OS_r0.78_L150	59.42	59.14	1.005	0.28
C/C_OS_r1.00_L75	48.69	48.79	0.998	0.10
C/C_OS_r1.00_L150	66.31	66.09	1.003	0.22
C/C_OS_r1.29_L75	48.13	48.02	1.002	0.09
C/C_OS_r1.29_L150	59.42	59.14	1.005	0.28
C/C_OS_r5.14_L75	29.42	29.35	1.002	0.07
C/C_OS_r5.14_L150	29.80	29.87	0.998	0.07
C/A_OS_r0.19_L75	26.19	26.20	1.000	0.01
C/A_OS_r0.19_L150	26.38	26.49	0.996	0.11
C/A_OS_r0.78_L75	42.61	42.26	1.008	0.35
C/A_OS_r0.78_L150	46.03	45.48	1.012	0.55
C/A_OS_r1.00_L75	43.87	43.59	1.006	0.28
C/A_OS_r1.00_L150	50.56	49.90	1.013	0.66
C/A_OS_r1.29_L75	42.61	42.26	1.008	0.35
C/A_OS_r1.29_L150	46.03	45.48	1.012	0.55
C/A_OS_r5.14_L75	26.19	26.20	1.000	0.01
C/A_OS_r5.14_L150	26.38	26.49	0.996	0.11
C/C_TS_r0.19/r0.78_L150	56.33	56.10	1.004	0.13
C/C_TS_r0.19/r1.00_L150	61.86	61.96	0.998	0.10
C/C_TS_r0.19/r1.29_L150	68.19	68.69	0.993	0.50
C/C_TS_r0.19/r5.14_L150	71.14	71.58	0.994	0.44
C/C_TS_r0.78/r1.00_L150	66.33	66.03	1.005	0.30
C/C_TS_r0.78/r1.29_L150	73.28	73.06	1.003	0.22
C/C_TS_r0.78/r5.14_L150	69.04	68.56	1.007	0.48
C/C_TS_r1.00/r1.29_L150	66.37	66.02	1.005	0.35
C/C_TS_r1.00/r5.14_L150	62.26	62.19	1.001	0.07
C/C_TS_r1.29/r5.14_L150	56.44	56.09	1.006	0.35
C/A_TS_r0.19/r0.78_L150	45.22	44.61	1.014	0.61
C/A_TS_r0.19/r1.00_L150	49.53	48.94	1.012	0.59
C/A_TS_r0.19/r1.29_L150	54.49	53.78	1.013	0.71
C/A_TS_r0.19/r5.14_L150	55.33	56.29	0.983	0.96
C/A_TS_r0.78/r1.00_L150	50.41	49.66	1.015	0.75
C/A_TS_r0.78/r1.29_L150	55.55	54.66	1.016	0.89
C/A_TS_r0.78/r5.14_L150	56.81	56.88	0.999	0.07
C/A_TS_r1.00/r1.29_L150	50.89	50.44	1.009	0.45
C/A_TS_r1.00/r5.14_L150	49.26	49.23	1.001	0.03
C/A_TS_r1.29/r5.14_L150	43.28	42.75	1.012	0.53

where E is the normal tensile modulus of the adherend, s_{max} is the shear displacement at maximum bond stress, w is the width of the joint (50 mm), t is the thickness of the material and R is the radius of circular particles in the model (0.5 mm). The shear stiffness defined in Eq. (9) matches the bilinear bond-slip model shown in Fig. 1a. The contact breaks in the normal direction when the maximum normal tensile force is attained

$$F^{n}_{max} = \sigma^{n}_{max} \cdot w \cdot t \tag{10}$$

whereas in the shear direction, the contact breaks when the maximum shear displacement (s_f) of 0.12 mm is reached and the shear force is null (see Fig. 1b). To compare the results between DEM and FEM models, the shear and normal stresses were obtained by dividing the contact force by an equivalent area, i.e. $t \times w$ for normal stress and $2R \times w$ for shear stress.

Similar to what was described in the FEM, no contact was assumed within the interfaces of the joints perpendicularly positioned with the loads. For the simplicity of the models, the distortion of the adherends was ignored by assuming that the shear stiffness of the contacts within the same material has a very high value (1×10^5 GPa). In addition, the displacement of particles along the y-axis were blocked. Therefore, based on the representation of DEM models of one and two-stepped joints shown in Fig. 4, the normal force and displacement relationship (F^n-U) simulates the elastic contacts between particles of materials 1 and 2 whilst the shear force and displacement relationship (F^s-s) simulates the interface elements between the two adherends and within the same material for the two-stepped joints, though, for the latter, the shear contact is nearly rigid.

The monotonic loading applied to the bonded joints was implemented in a displacement-control mode by imposing a constant displacement speed of 4 mm/s to the first particle of the layer on the left of material 1 (see Fig. 4). Moreover, the displacements in the direction of the x-axis of most right-hand side particles of material 2 were blocked. The adopted calculation time step was 1×10^{-10} s.

5. Results and discussions

This section presents and discusses the results obtained from the numerical simulations. The following three main topics are addressed: (a) the load capacities of the stepped joints; (b) the relationship between the loads transmitted to the stepped joints and the interfacial slips at the loaded edge of the joints; and (c) the bond stress distributions throughout the bonded lengths in which the identification and description of the debonding processes are also presented.

5.1. Load capacities of the stepped bonded joints

The load capacities of the models are summarized in Table 2. The absolute deviation between the numerical simulations presented in this table was calculated as follows:

$$AD = \left| F^{(FEM)}_{max} - F^{(DEM)}_{max} \right| \tag{11}$$

where $F^{(FEM)}_{max}$ and $F^{(DEM)}_{max}$ are the maximum loads of the specimen obtained in the FEM and the DEM, respectively. The calculated absolute deviations never exceeded 1.00 kN and ranged between 0.01 kN (in specimen C/A_OS_r0.19_L75) and 0.96 kN (in specimen C/A_TS_r0.19/r5.14_L150). The mean absolute deviation obtained from both numerical methods is 0.35 kN, which reveals the good agreement between methods.

The load capacity varied significantly with the joint characteristics such as type of joint, bonded length, materials and thicknesses [10,18]. For instance, for the one-step bonded joint the effect of increasing the bonded length from 75 mm to 150 mm was nearly insignificant in some situations (e.g. in specimens C/C_OS_r0.19_L75 and C/C_OS_r0.19_L150), whereas in other situations (e.g. in specimens C/C_OS_r1.00_L75 and C/C_OS_r1.00_L150) it was very important. This can be explained by the effective bond length of the joint, which increases with the axial stiffness ratio and it is maximized when $r = 1$ [26]. Therefore, such differences between specimens with different r values is due to an insufficient bonded length of the specimens C/C_OS_r1.00_L75 and C/C_OS_r1.00_L150 when compared with those with $r = 0.19$. Also, the C/C series demonstrated a higher load capacity than the homologous C/A series regardless of the joint characteristics.

Looking at the one-step bonded joints with a total length of 150 mm, it can be seen that the models with the highest load capacity were the ones where $r = 1.00$ was assumed. At the opposite end of the scale, the models with $r = 0.19$ are associated with the lowest debonding loads. As will be seen later when $r = 1.00$ the debonding process is symmetric, which means that the softening stage appears on both edges of the joint, so, due to equilibrium conditions, the load capacity of those joints should be the highest. From another perspective, the two-step joints combining $r = 1.00$ and $r \neq 1.00$ never led to significantly higher debonding loads, which may indicate that, from the load capacity point of view, no benefit is derived from adding a second step to joints with $r = 1.00$ in part of it.

5.2. The load-slip curves

To analyse the load-slip curves of these first numerically simulated specimens, the interfacial slips were calculated according to Eq. (5) and they represent the relative displacement between adherends at both ends of the joints. The results were grouped into the one-step joints and two-step joints of the C/C and C/A series. The former are shown in Fig. 5. The interfacial slips on the extreme left and right-hand sides were plotted, respectively, on the left and right of the individual plots using different colour lines (blue and red). The load-slip curves obtained from the FEM and the DEM are quite similar. Both methods have predicted that when $r < 1$ the debonding of

the specimens begins from the left of the joint towards the right, but when $r > 1$ the debonding initiates on the right-hand side of the joint, it develops towards the left. However, when $r = 1$, the debonding is initiated at both edges of the joint at the same time. These are consistent with the analytical findings available in the literature [26]. It should be mentioned that despite specimen C/A_OS_r1.00_L150 having an axial stiffness ratio equal to $r = 1$, the debonding was not perfectly symmetric, as would have been expected. The main cause for this is the approximation used to model the thicknesses of this joint, i.e. by using $t_{a1} = 1.57$ mm and $t_{a2} = 4.03$ mm we have an axial stiffness of 0.998, which, being lower than 1, induces the debonding on the left-hand side of the joint slightly before it starts on the right. Between $r = 0$ and 1, the results also show that the bond capacities of the joints increase with the increase of r.

At the edge of the joints where debonding has initiated, the load-slip curves show three different trends. In the first one, which is at low load magnitudes, the load-slip relationship has a linear behaviour that is followed by a nonlinear branch. If the linear behaviour is due to the linear behaviour of the interface, the nonlinear behaviour of the load-slip curve is a consequence of the appearance of the softening within the interface. As the load tends towards a steady plateau, the complete separation between adherends has begun and it will be proportional to the total bonded length of the joint. This also shows that the joint has a sufficient bonded length, which allows it to reach the maximum load capacity. In other words, the bonded length of the joint is longer than the effective bonded length of the joint, i.e. the length beyond which no further load can be transmitted to the joint [26,63–65].

Another aspect that can be seen from Fig. 5 is that by decreasing the elastic modulus of one adherend, the load capacity of the joint decreases. Looking at the load-slip curves obtained from the two-step bonded joints shown in Figs. 6 and 7 the same trend is observed. For instance, by comparing the maximum load capacity of specimens C/C_OS_r1.00_L150 and C/A_OS_r1.00_L150, it can be seen that the former has 16 kN of load capacity more than the latter specimen. These results suggest that the use of higher elastic modulus materials may contribute to obtaining stronger bonded joints, which also justifies the use of CFRP composites in the development of hybrid bonded joints independently of their configuration, whether they have one or two steps.

To facilitate the comparison between the two-step and one-step bonded joint configurations, in Figs. 6 and 7 the load-slip curves of two-step joints are plotted against the curves of one-step joints with a total bonded length of 150 mm and with an axial stiffness equal to r_a or r_b. For instance, in Fig. 6a, the load-slip curves obtained from specimen C/C_TS_r0.19/r0.78_L150 are compared with the load-slip curves (in grey) of specimens C/C_OS_r019_L150 and CC_OS_r0.78_L150. In this case, the two-step configuration initially followed the same results as the specimen C/C_OS_r0.78_L150 but since it is only 75 mm long, it did not reach the same maximum load as the one-step joint specimen. However, unlike the one-step joint configuration that dropped to zero after reaching the maximum load, the load in the two-step configuration dropped to a maximum load value lower than that reached in the one-step joint configuration with $r_a = 0.19$. Consequently, the debonding initiated on the left-hand side of the two-step joint. It should also be mentioned that the numerical simulations carried out in this work are not able to predict the snapback behaviour of the joints as described in the literature for other types of joint configurations [26,37,50,60,66–68] and therefore, the interfacial slips all have a monotonic trend.

Another particularity that can be observed from Figs. 6 and 7 is the anti-symmetry found between eight specimens (four specimens per series). If we consider the C/C series, the load-slip curves of specimens C/C_TS_r0.19/r0.78_L150, C/C_TS_r0.19/r1.00_L150, C/

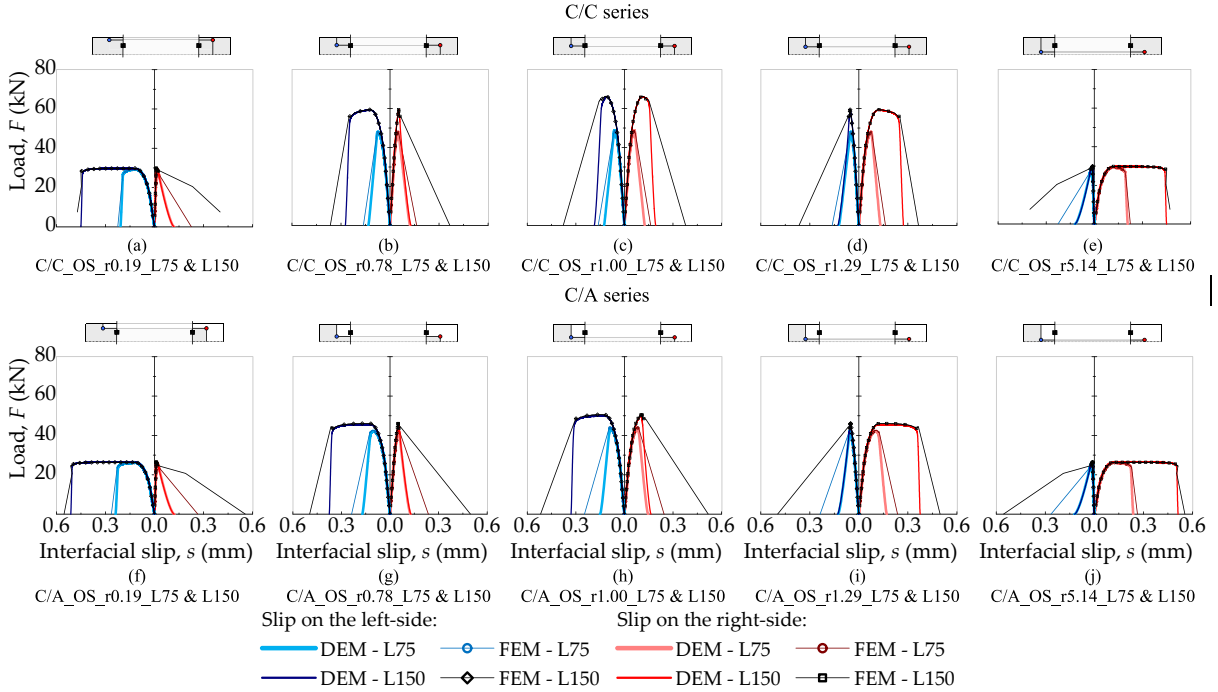

Fig. 5. Load-interfacial slip curves of the one-step bonded joints.

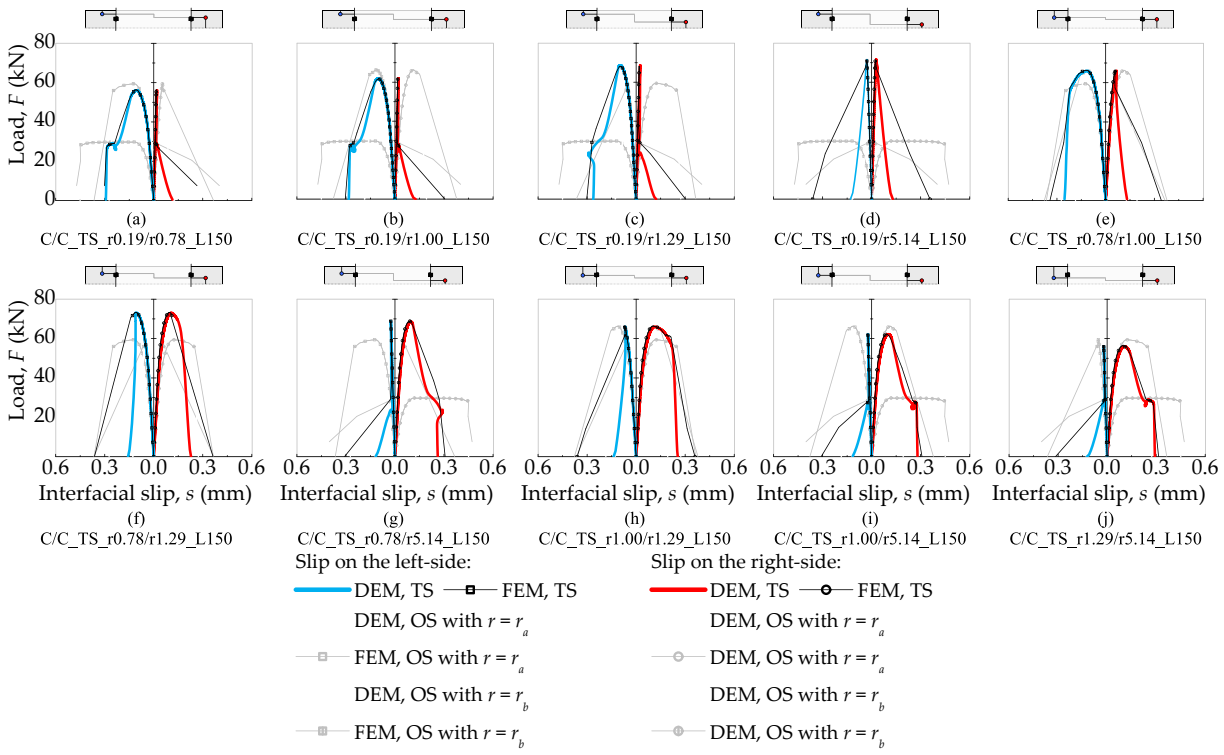

Fig. 6. Load-interfacial slip curves of the two-step bonded joints (CFRP-to-CFRP joints) with a total bonded length of $L_t = 150$ mm.

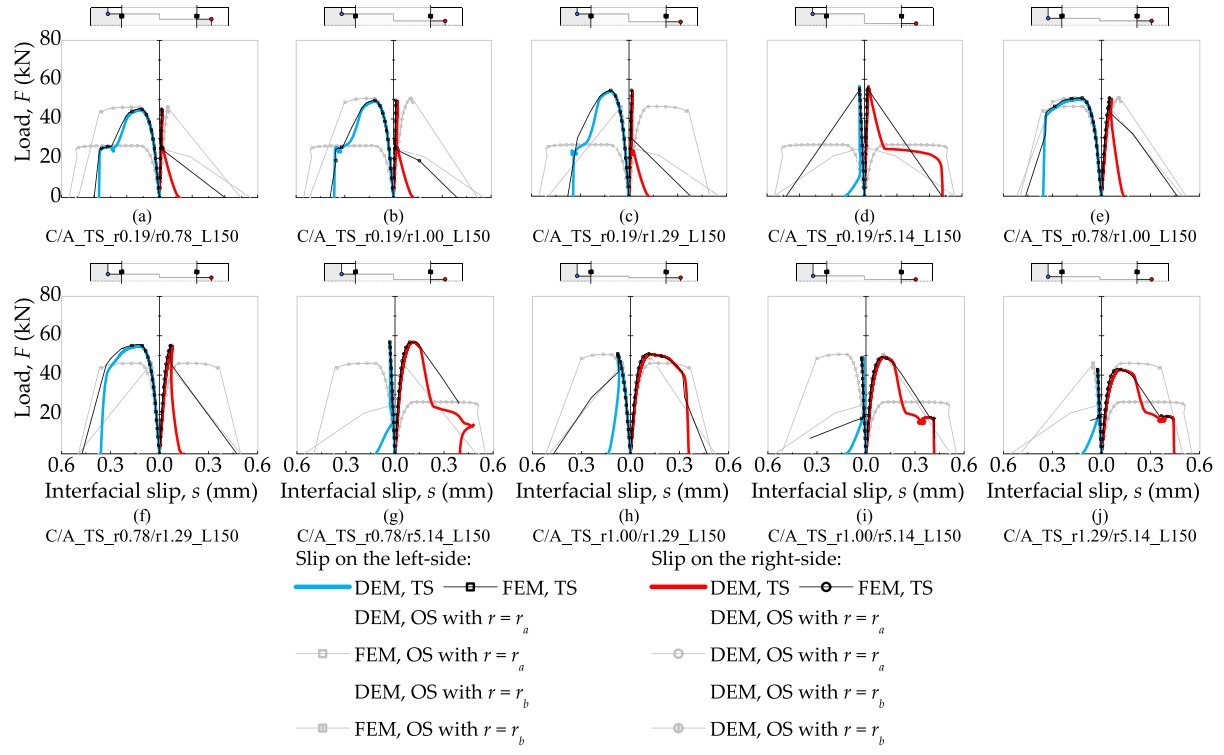

Fig. 7. Load-interfacial slip curves of the two-step bonded joints (CFRP-to-aluminium joints) with a total bonded length of $L_t = 150$ mm.

C_TS_r0.19/r1.29_L150 and C/C_TS_r0.78/r1.00_L150 are similar, but the exact opposite of those observed in specimens C/C_TS_r1.29/r5.14_L150, C/C_TS_r1.00/r5.14_L150, C/C_TS_r0.78/r5.14_L150 and C/C_TS_r1.00/r1.29_L150, respectively. This allows us to asseverate that the debonding process of a two-step joint with a generic r_a and r_b will be the same but in the opposite direction, of a second two-step joint with a r_a equal to $1/r_b$ of the first joint and r_b equal to $1/r_a$ of the first joint. For instance, specimen C/C_TS_r0.19/r0.78_L150 should have the same debonding process (but in the opposite direction) as specimen C/C_TS_r1.29/r5.14_L150.

5.3. The bond stresses on the one-step joints

The description of the debonding process of the one-step joints is presented in this subsection. To allow us to describe the debonding processes of joints, the three stages defined in the local bond behaviour of the interface (see Fig. 1b) must be considered. Therefore, all the different states that the interfaces of the one-step joints will undergo until their complete failure will be defined by the E, S and D stages or by a combination of these three. Also, it is assumed that before any loads have been applied to the joint its initial state will be the Undeformed (U) state.

The following slips at the most loaded end were selected to show the bond stress distributions throughout the total bonded length of the joints: (a) Point A where $s = 0.026$ mm, Point B where $s = 0.050$ mm, Point C where $s = 0.075$ mm, Point D where $s = 0.120$ mm, and Point E where $s = 0.200$ mm. For these one-step bonded joints, three different cases can also be identified: (a) $r_a < 1$; (b) $r_a = 1$; and (c) $r_a > 1$. Each of these is discussed thoroughly next. Moreover, to facilitate the identification and description of the debonding processes of the one-step joints, only the results obtained from the specimens with a total length of 150 mm are reported here.

5.3.1. Cases with $r_a < 1$

For an axial stiffness lower than 1, two different cases can be observed during the debonding process of the one-step joints. The first case can be identified when the axial stiffness value is quite low (i.e. 0.19), whereas the other case will correspond to an axial stiffness ratio close to 1. In the former case, the bond stresses developed on the right-hand side of the joint never reach the S stage (see Fig. 8a and 8b), whilst in the interface of the latter case a region developing the S stage can be seen on the right of the joint (see Fig. 8c and 8d). Therefore, the debonding sequences of these joints follow a different path. Moreover, to facilitate the identification of each stage (E, S and D) on the states that the interface develops for the five nominated slips, Fig. 8b gives an example of the D-S-E state developed in specimen C/A_OS_r0.19_L150 at $s = 0.200$ mm.

In the case of the one-step joints with $r_a = 0.19$, at very low load magnitudes, the interface is under an E-U-E state that rapidly tends to an E state with a small increase in the loads. Moreover, the magnitude of the bond stresses on the left of the joint is higher than that developed on the opposite side. Therefore, the E state ends when the maximum bond stress (τ_{max}) is reached on the left edge of the joint ($s = 0.026$ mm). On this side, the bond stresses tend now to decrease while the position where τ_{max} develops migrates to the right side of the joint. This may describe the S-E state of the joint and once it maximizes the bond stresses within the interface, i.e. immediately before the full separation between adherends, its limit will lead to the load capacity of the joint. The next state is the D-S-E state (see the curve at $s = 0.200$ mm), which means that the full debonding between adherends has already begun on the left of the joint since no

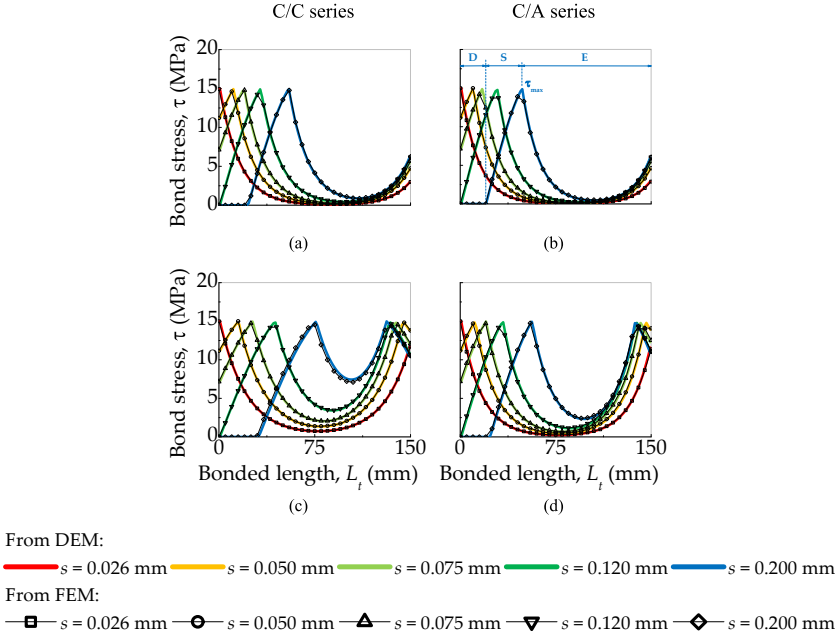

Fig. 8. Distributions of the interfacial bond stresses in specimens: (a) C/C_OS_r0.19_L150; (b) C/A_OS_r0.19_L150; (c) C/C_TS_r0.78_L150; and (d) C/A_TS_r0.78_L150.

bond stresses are now being transferred between adherends. Despite not being shown in Fig. 8, the next states are the D-S and D states, in that order.

If we now consider the case with $r_a = 0.78$, the debonding sequence until its failure follows these seven states: (a) E-U-E; (b) E; (c) S-E; (d) S-E-S; (e) D-S-E-S; (f) D-S; and (g) D. As in the previous case, the E-U-E is almost marginal and, despite always corresponding to very low load magnitudes, it may be more meaningful if the total bonded length is quite long. Although in the E state, the bond stresses are all lower than τ_{max}, the left-hand side of the joint develops the highest bond stresses. So, the limit of the E state is reached when τ_{max} is reached on the left-hand side of the joint. After this state, the S stage defined in Fig. 1b will occur on this same edge. Next, the S-E-S state appears (curves $s = 0.050$ mm, 0.075 mm and 0.120 mm), which means that the interface of the joint develops another S region within the interface localized on the right-hand side of the joint and, therefore, the S stage can be observed on both edges of the joint. Since the S stage on the left of the joint is more advanced than on the right, the complete separation between adherends, i.e. the D stage defined in Fig. 1b, will occur on the left-side of the joint leading to the D-S-E-S state. At the beginning of this state, the bond stress configuration is maximized, and the load capacity of the joint is reached. From the point of view of the equilibrium of the adherends, since the bond stresses obtained in these joints have a larger area than those obtained in the joints with $r_a = 0.19$, the bond capacities of the joints with a $r_a = 0.78$ are higher than those obtained from the joints with $r_a = 0.19$. Afterwards, with the full debonding between materials, the loads tend to decrease, and the following states are associated with lower loads.

These debonding processes are like those observed for double-overlap bonded joints [26]. Since the debonding processes of these bonded joint configurations are very much alike, it means that the bond capacities of both are the same.

5.3.2. *The case with $r_a = 1$*

In this case, the sequence of the debonding process is quite similar to that already explained for the case when $r_a = 0.78$. However, in this case where $r_a = 1$, one main aspect should be considered: the debonding process should follow a symmetric path. Despite not being entirely verified in specimen C/A_r1.00_L150, as explained previously (with $r_a = 0.998$), this symmetry is quite visible from Fig. 9a. So, the debonding process of these cases will follow the six states until their failure: (a) E-U-E; (b) E; (c) S-E-S; (d) D-S-E-S-D; (e) D-S-D; and (f) D. Bearing in mind the symmetry of this case, the first three states are similar to the homologous states described for the one-step joint with $r_a = 0.78$. However, the end of the E state and the beginning of the S-E-S is carried out when τ_{max} is reached on both edges of the joints. Then, the S stage increases in the same proportions on both edges of the joints. The end of this state corresponds to the full debonding between adherends on both edges of the joint and at this point, the development of the interfacial bond stresses is maximized, which also means that the load capacity of the joint is reached. Since in these cases, the largest areas of bond stress are obtained, these are the cases with the highest bond capacities. With the progression of the D-S-E-S-D state, the loads tend now to decrease. It should be mentioned also that the D-S-E-S-D is not shown in Fig. 9a because no data were obtained for Point E (with $s =$ 0,200 mm). Although the following states cannot be visible in Fig. 9, the E region localized in the centre of the one-step joint will disappear and when it does, the D-S-D develops within the interface. In the end, the D state will correspond with no loads transmitted to the joint and the adherends are now completely separated from each other.

5.3.3. *Cases with $r_a > 1$*

These cases fall into the one-step joint with $r_a = 1.29$ and 5.14. Since $1/r_a = 1/1.29 = 0.78$ or $1/r_a = 1/5.14 = 0.19$, debonding will initiate on the right-hand side of these joints rather than on the left. The debonding processes of these one-step joints are the same as those previously described in 5.3.1 but with the first appearance of the S and D stages within the interface on the right-hand side of the joints. Therefore, to avoid increasing the text unnecessarily, the distributions of the bond stresses obtained from these specimens are not shown since they can be also obtained from those shown in Fig. 8.

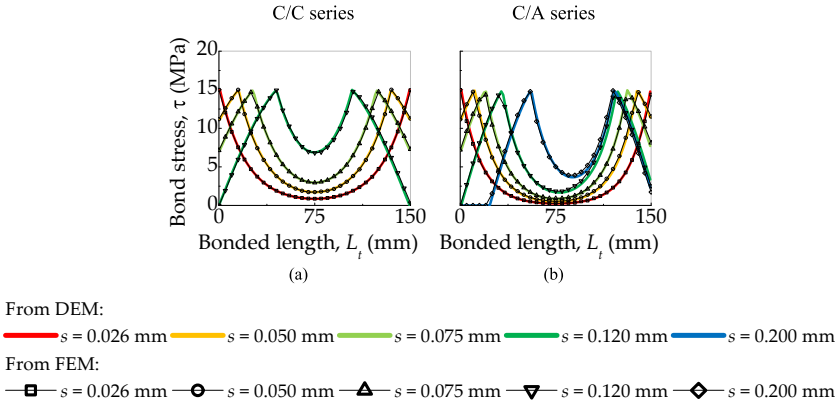

Fig. 9. Distributions of the interfacial bond stresses in specimens: (a) C/C_OS_r1.00_L150; and (b) C/A_OS_r1.00_L150.

5.4. The bond stresses on the two-step joints

Like the one-step bonded joints, the understanding of the debonding process of the two-step joints is carried out by bearing in mind the three stages (E, S, and D), initially assumed for the local bond behaviour shown in Fig. 1b. Depending on the axial stiffness in the two parts of the joint, the interface will show different bond stress distributions until failure. Therefore, this section presents the interfacial bond stresses that the different two-step joints may have until their failure for five possible cases with: (i) $r_a < 1$ and $r_b < 1$; (ii) $r_a < 1$ and $r_b = 1$; (iii) $r_a < 1$ and $r_b > 1$; (iv) $r_a > 1$ and $r_b > 1$; and (v) $r_a = 1$ and $r_b > 1$. To facilitate the correspondence with the load-slip curves of the two-step bonded joints, the same five points (Points A to E) previously selected in Subsection 5.3 were considered once again.

5.4.1. The case with $r_a < 1$ and $r_b < 1$

This case includes specimens C/C_TS_r0.19/r0.78_L150 and C/A_TS_r0.19/r0.78_L150. Fig. 10 shows the bond stresses associated with these two-step joints at the five previous nominated slips. The results revealed that debonding initiates on the left-hand slide of the joint, i.e. where the stiffness ratio r_a is lower than the stiffness ratio r_b. Although not shown in Fig. 10, the first state of the joint would be the E-U-E/E-U-E state and it would correspond to quite a low load magnitude transmitted to the joint. In these two cases, the bond stresses corresponding to Point A ($s = 0.026$ mm) represent the upper limit of the E/E state. In this state, it is already visible that the maximum bond stress (τ_{max}) is localized at the left edge of the two-step joint. With the increase of the loads, the Softening of the interface appears on the left edge of the joint and maximum bond stress moves towards the right of the joint. The identification of the Softening of the interface can be carried out by identifying the region where the bond stresses decrease from their maximum value. Therefore, this state is S-E/E and it will end when the Softening region is maximized, i.e. when the bond stress becomes zero. After this point, the D-S-E/E state is initiated, and the two-step joint reaches its maximum load capacity. In the next states, the load transmitted to the joint decreases. So, the next state to be developed within the interface is the D-S/E and D-S/S-E states, respectively. In the latter, the interface on the right-hand side of the joint has developed the S stage and the interfacial maximum bond stress can also be seen on this side of the joint. Since the next states have an interfacial slip higher than that adopted for Point E ($s = 0.200$ mm), these states are not shown in Fig. 10. Still, the following expected states can be identified as the D/S-E state and the D/D-S state, respectively. Corresponding to the instant that no loads are transmitted to the interface, i.e. when the adherends have completely separated from each other, the D/D state (or simply the D state) is the last state of these joints.

5.4.2. The case with $r_a < 1$ and $r_b = 1$

The description of the debonding process of this case is based on the specimens C/C_TS_r0.19/r1.00_L150, C/C_TS_r0.78/r1.00_L150, C/A_TS_r0.19/r1.00_L150 and C/A_TS_r0.78/r1.00_L150. From the distributions of the interfacial bond stresses shown in Fig. 11, specimens in the C/A series have developed an S stage on the right-hand side of the joint during their debonding processes, whilst specimens in the C/C series have developed only the E stage on that side of the joint. Therefore, the axial stiffness ratio between adherends influenced the debonding of these two-step joints, i.e. the results suggest that increasing the stiffness ratio of the right-hand side of the two-step joints (r_b) allows them to develop an S stage on both edges of the joint.

In this context, the debonding process of the specimens of the C/C series (see Fig. 11a and 11c) is the following until failure: (a) E-U-E/E-U-E; (b) E/E (or, for simplicity, E); (c) S-E/E; (d) D-S-E/E; (e) D-S/E; (f) D-S/S-E; (g) D/D-S-E; (h) D/D-S; and (i) D/D (or D). On the other hand, the specimens from the C/A series (see Fig. 11b and 11d) revealed the following debonding path until failure: (a) E-U-E/E-U-E; (b) E/E (or only E); (c) S-E/E; (d) S-E/E-S; (e) D-S-E/E-S; (f) D-S/S-E-S; (g) D/S-E-S; (h) D/S; and (i) D/D (or only D).

As had occurred in the one-step bonded joints with $r_a = 0.19$ and 0.78, in all these specimens the debonding initiation began from the left-hand side of the two-step joints in which the axial stiffness ratio is lowest, i.e. from where $r_a = 0.19$ and 0.78. Another particularity of these joints is the occurrence of larger areas under the bond stress distributions on the left-hand side of the joints. Unlike the one-step bonded joints with $r_a = 1$, where the interfaces developed the largest areas of bond stresses, the left-hand side of these two-

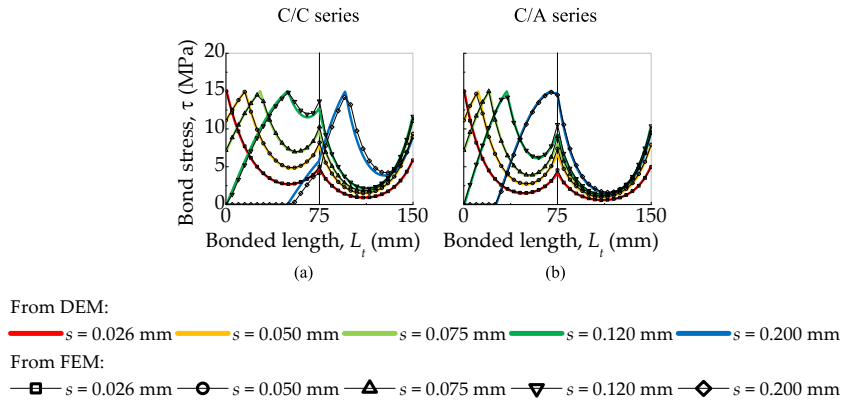

Fig. 10. Distributions of the interfacial bond stresses in specimens: (a) C/C_TS_r0.19/r0.78_L150; and (b) C/A_TS_r0.19/r0.78_L150.

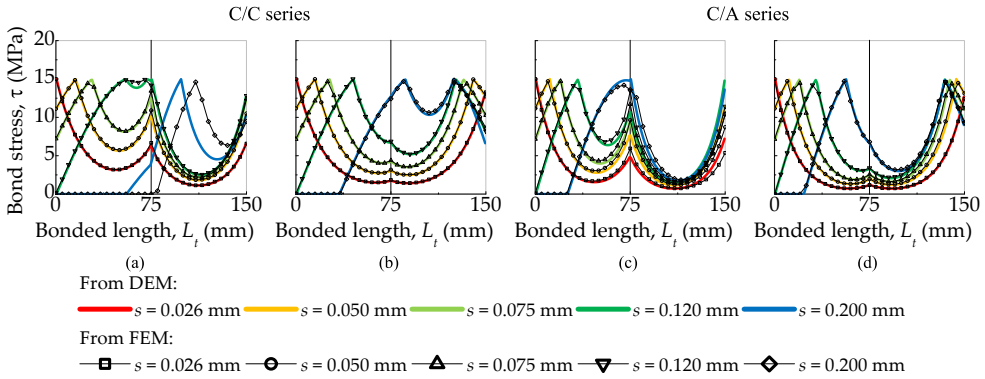

Fig. 11. Distributions of the interfacial bond stresses in specimens: (a) C/C_TS_r0.19/r1.00_L150; (b) C/C_TS_r0.78/r1.00_L150; (c) C/A_TS_r0.19/r1.00_L150; and (d) C/A_TS_r0.78/r1.00_L150.

step joints now seems to contribute greatly to the load capacity of the joints.

It should be noted also that both numerical methods have very close predictions for the five bond stress distributions shown in each case (see Fig. 11). Nevertheless, some differences can be found on Point E (with $s = 0.200$ mm) of specimen C/C_TS_r0.19/r1.00_L150 since, after the post-peak load, the closest slip obtained from the FEM was $s = 0.233$ mm. Therefore, it justifies why the D-S/S-E state obtained from the DEM corresponds to a different state obtained from the FEM in which a more advanced state (D/D-S-E) was obtained.

5.4.3. The case with $r_a < 1$ and $r_b > 1$

This is the case that covers a broader range of specimens in this study: C/C_TS_r0.19/r1.29_L150, C/C_TS_r0.19/r5.14_L150, C/C_TS_r0.78/r1.29_L150, C/C_TS_r0.78/r5.14_L150, and their corresponding homologous specimens of C/A series. Four debonding processes can be identified from the bond stress distributions shown in Fig. 12. Therefore, for specimens C/C_TS_r0.19/r1.29_L150 (see Fig. 12a) as well as for the homologous one from the C/A series (see Fig. 11e), the debonding sequence is identical to that already identified in Subsection 5.4.2 for specimens C/C- and C/A_TS_r0.19/r1.00_L150 (see Fig. 11a and 11c, respectively). In this case, the differences observed at Point E between the results obtained from the DEM and the FEM occur because the closest data obtained from the FEM to the nominated slip of 0.200 mm is 0.245 mm in the C/C specimen (Fig. 12a) and 0.183 mm in the C/A specimen (Fig. 12e). Consequently, the bond stress configuration at that nominated point obtained from the FEM corresponds to a point where the

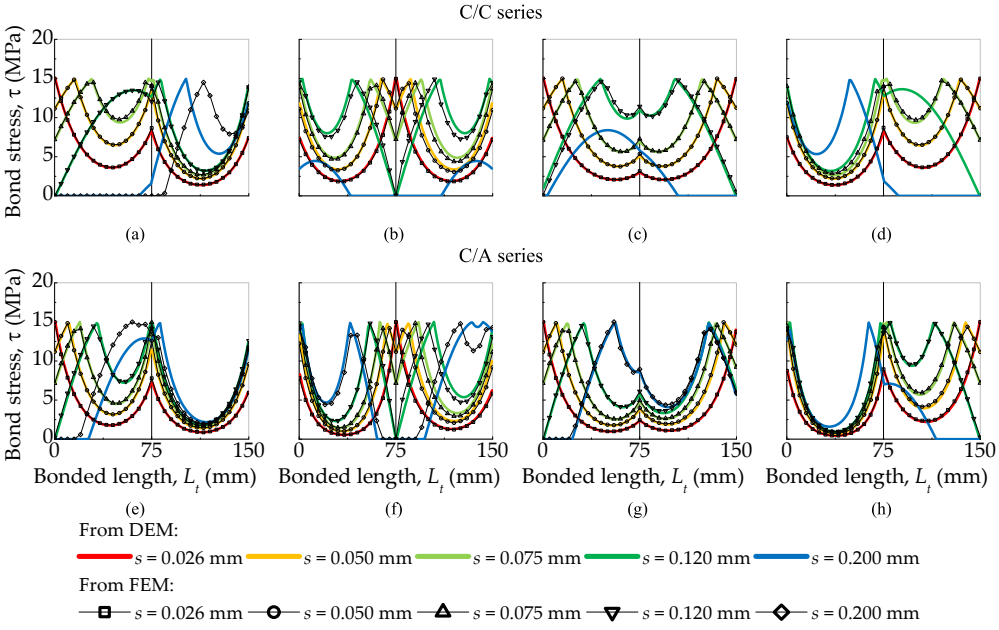

Fig. 12. Distributions of the interfacial bond stresses in specimens: (a) C/C_TS_r0.19/r1.29_L150; (b) C/C_TS_r0.19/r5.14_L150; (c) C/C_TS_r0.78/r1.29_L150; (d) C/C_TS_r0.78/r5.14_L150; (e) C/A_TS_r0.19/r1.29_L150; (f) C/A_TS_r0.19/r5.14_L150; (g) C/A_TS_r0.78/r1.29_L150; and (h) C/A_TS_r0.78/r5.14_L150.

debonding of the interface of the C/C specimen is in a more advanced state. For this same reason, the bond stress configuration obtained from the FEM of the C/A specimen corresponds to an earlier debonding state (although not much different) from that obtained from the DEM, where the results correspond exactly to $s = 0.200$ mm. Based on the numerical results, the path that the two-step joint undergoes until failure is as follows: (a) E-U-E/E-U-E; (b) E/E (or only E); (c) S-E/E; (d) D-S-E/E; (e) D-S/S-E; (f) D/S-E; (g) D/S; and (h) D/D (or only D).

The second debonding process that can be identified here is the one that is observed in specimen CC_TS_r0.19/r5.14_L150. In this situation, the results suggest that the debonding process has a symmetric configuration to the centre of the joint. Moreover, the debonding initiates at the centre of the joint in these specimens, i.e. between the transition from the left to the right side of the joint. Considering the results shown in Fig. 12b and 12f, the debonding processes in these specimens follow this sequence until failure: (a) E-U-E/E-U-E; (b) E/E (or only E); (c) E-S/S-E; (d) S-E-S/S-E-S; (e) S-E-S-D/D-S-E-S; (f) S-D/D-S; and (g) D/D (or only D).

Specimens C/C_TS_r0.78/r1.29_L150 and C/A_TS_r0.78/r1.29_L150 are now used to describe the third debonding process. Although $r_a = 1/r_b$, in these two cases, debonding initiates on both edges of the joints and propagates towards the centre. This means that unlike specimens C/C_TS_r0.19/r5.14_L150 and C/A_TS_r0.19/r5.14_L150, the maximum bond stresses first develop on both edges of the joint. The softening stages also develop first on the edges and with the increase in the load transmitted to the joint, the maximum bond stresses also migrate from the edges to the centre of the joints. From the results shown in Fig. 12c and 12 g, the debonding processes of these joints undergo the following paths until failure: (a) E-U-E/E-U-E; (b) E/E (or only E); (c) S-E/E-S; (d) D-S-E/E-S-D; (e) D-S/S-D; and (f) D/D (or only D).

Finally, to describe the fourth debonding process, specimens C/C_TS_r0.78/r5.14_L150 and C/A_TS_r0.78/r5.14_L150 are considered. In this case, their corresponding debonding processes are very similar to the specimens C/C_TS_r0.19/r1.29_L150 and C/A_TS_r0.19/r1.29_L150. The main difference is the direction that the debonding process takes, i.e. instead of debonding taking place on the left-hand side of the joint (see Fig. 12a and 12e), it begins on the right (see Fig. 12d and 12 h). Therefore, the bond stress configurations obtained from specimens C/C_TS_r0.78/r5.14_L150 and C/A_TS_r0.78/r5.14_L150 shown in Fig. 12d and 12 h are symmetric with those in the specimens shown in Fig. 12a and 12e. In this case, the corresponding debonding sequence until failure obtained from the numerical simulations is: (a) E-U-E/E-U-E; (b) E/E (or only E); (c) E/E-S; (d) E/E-S-D; (e) E-S/S-D; (f) E-S/D; (g) S/D; and (h) D/D (or only D).

5.4.4. *The case with $r_a > 1$ and $r_b > 1$*

As already explained, by swapping the stiffness ratios of the joints from the right to the left and *vice versa*, and calculating their inverse value, the debonding process is also swapped. Therefore, the bond stress distributions in specimens C/C_TS_r1.29/r5.14_L150 and C/A_TS_r1.29/r5.14_L150, shown in Fig. 13, are very similar to those obtained in specimens C/C_TS_r0.19/r0.78_L150 and C/A_TS_r0.514/r0.78_L150, respectively (see Fig. 10). Unlike specimens C/C_TS_r0.19/r0.78_L150 and C/A_TS_r0.514/r0.78_L150, where the debonding initiated on the left-hand side of the joint, in these specimens with $r_a > 1$ and $r_b > 1$, the debonding begins on the right-hand side of the joint and follows the same states until failure.

In this case, the first side of the joint to debond is the one with the highest stiffness ratio ($r_b = 5.14$) which means, compared with the one-step bonded joint with $r_a = 5.14$, the debonding initiates on the same side (right) and the associated load capacity is lower than that of the one-step joint with $r_a = 1.29$. Consequently, and considering the equilibrium of one adherend, it would be expected that the two two-step joints from the C/C series should have the same load capacity, and the same should occur on the other two two-step joints in the C/A series (see Table 2).

5.4.5. *The case with $r_a = 1$ and $r_b > 1$*

Four specimens fall into this case: C/C_TS_r1.00/r1.29_L150, C/C_TS_r1.00/r5.14_L150, C/A_TS_r1.00/r1.29_L150, and C/A_TS_r1.00/r5.14_L15. Fig. 14 shows the predicted bond stress distributions of these specimens for the nominated slips. By swapping the axial stiffness ratio from the right (r_b) to the left (r_a) and *vice versa*, and inverting the corresponding values of the axial stiffnesses,

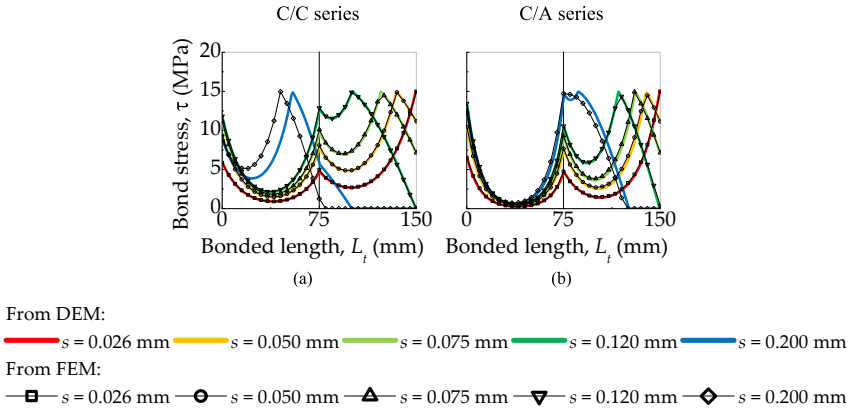

Fig. 13. Distributions of the interfacial bond stresses in specimens: (a) C/C_TS_r1.29/r5.14_L150; and (b) C/A_TS_r1.29/r5.14_L150.

the debonding processes should be similar to those obtained in specimens C/C_TS_r0.78/r1.00_L150, C/C_TS_r0.19/r1.00_L150, C/A_TS_r0.78/r1.00_L150, and C/A_TS_r0.19/r1.00_L150, respectively. Therefore, the debonding sequences of these joints with $r_a = 1$ and $r_b > 1$ go in the opposite direction to the debonding sequences already discussed for the two-step joints with $r_a < 1$ and $r_b = 1$ (see Subsection 5.4.2). Furthermore, the load capacities of the joints from the C/C series with $r_a < 1$ and $r_b = 1$ should be the same as the joints in the same series with $r_a = 1$ and $r_b > 1$, and the same should occur for the specimens in the C/A series (see Table 2).

6. Identification of the Two-Step joint optimized geometry

As previously shown, the configurations of the two-step bonded joints that led to the highest bond strengths had a relationship between the axial stiffness ratios on the left (r_a) and right (r_b) sides of the joint, such as $r_a = 1/r_b$. This led to two different debonding processes, i.e. one where the debonding initiated at the centre of the joint and propagated towards the edges and another where the debonding began from both edges and propagated towards the centre of the joint. However, the previous cases may not correspond to the two-step joint configuration with the highest load capacity. Therefore, the present parametric study aims to identify the best two-step joint configuration that leads to the highest load capacity. To do so, 13 new configurations with $r_a = 1/r_b$ were created. Considering the influence of the elastic modulus of the adherends as well, 52 new numerical simulations (26 with FEM and another 26 with DEM) were carried out. Table 3 summarises the load capacities of these 26 new joints.

The results suggest that the highest bond capacities of the two-step joints are reached when $r_a = 1/3$ (and $r_b = 3$) for the C/C specimens and when r_a is approximately 0.31 (and $r_b = 3.23$) for the C/A specimens. Fig. 15a shows the normalized load capacities of the joints, i.e. the ratio between the maximum loads obtained in each simulation ($F_{\max,ra}$) and the maximum load obtained in those simulations where the specimens had the highest load capacities ($F_{\max}$). Fig. 15 shows this normalized load related to the parameter ξ, which is defined according to:

$$\xi = \frac{\left[t - t_{a2}\cdot\left(1+\frac{E_2}{E_1}\right)\right]\cdot\left(1+\frac{1}{r_a}\right)}{\left[t - t_{a2}^{F_{\max}}\cdot\left(1+\frac{E_2}{E_1}\right)\right]\cdot\left(1+\frac{1}{r_a^{F_{\max}}}\right)} \tag{12}$$

where $t_{a2}^{F\max}$ and $r_a^{F\max}$ are the thickness of material 2 and the axial stiffness ratio on the left-hand side for the two-step bonded joint with the maximized load capacity; and t is the thickness of the joint obtained from:

$$t = t_{a1} + t_{a2} = t_{b1} + t_{b2} \tag{13}$$

The estimation of the bond capacities of this type of joint configuration can be made by fitting the numerical results with the following equation:

$$F_{\max,ra} = \left(a - \frac{1}{1+e^{-b\cdot(\xi-c)}}\right)\cdot\frac{1}{1+e^{-d\cdot\xi}}\cdot F_{\max} \tag{14}$$

where a, b, c and d are dimensionless parameters obtained through a minimization process where the sum of the squared differences between the numerical values and those obtained from Eq. (14) is considered. In this minimization process, two constraints were considered that aimed to avoid Eq. (14) exceeding the highest load capacity of the joints, i.e. the values of $F_{\max,0,33}$ and $F_{\max,0,31}$ were set equal to 1. Consequently, $a = 1.487$, $b = 1.404$, $c = 1.452$ and $d = 1.964$ were obtained. So, when Eq. (14) is used to predict the maximum loads obtained in each numerical simulation, the results show very good agreement with absolute deviations lower than 10%, as can be seen from Fig. 15b. Therefore, the proposed model in (14) can be useful to precisely predict the maximum bond capacities of two-step bonded joints where the relationship between the axial stiffness ratio is $r_a = 1/r_b$.

Looking closely at the result obtained from the numerical model C/C_TS_r0.33/r3.00_L150, it can be seen that if the first step of the

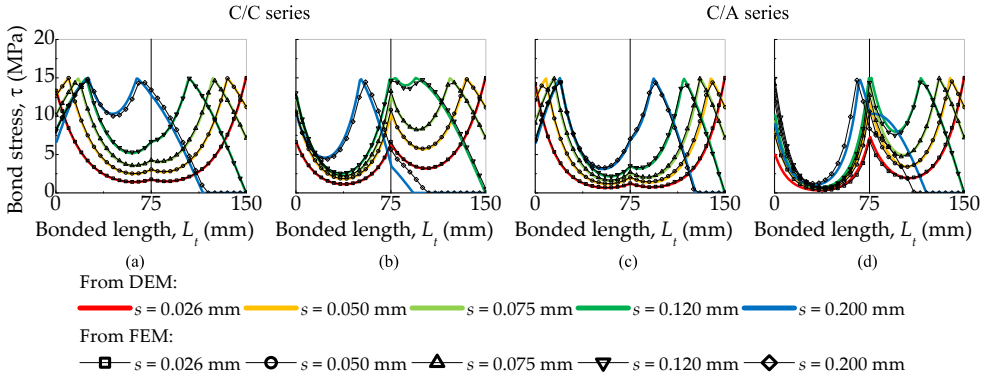

Fig. 14. Distributions of the interfacial bond stresses in specimens: (a) C/C_TS_r1.00/r1.29_L150; (b) C/C_TS_r1.00/r5.14_L150; (c) C/A_TS_r1.00/r1.29_L150; and (d) C/A_TS_r1.00/r5.14_L150.

Table 3
Bond capacities of the two-step bonded joints with $r_a = 1/r_b$.

Numerical model	Elastic modulus (GPa) Mat. 1 | Mat. 2	Thickness (mm) t_{a1} & t_{a2} | t_{b1} & t_{b2}	FEM (kN)	DEM (kN)	$F_{max}^{(FEM)}/F_{max}^{(DEM)}$	Absolute deviation (kN)
C/C_TS_r0.10/r10.0_L150	180 | 180	5.09 & 0.51 | 0.51 & 5.09	47.32	47.27	1.001	0.05
C/C_TS_r0.12/r8.33_L150		5.00 & 0.60 | 0.60 & 5.00	52.51	52.74	0.996	0.23
C/C_TS_r0.15/r6.67_L150		4.87 & 0.73 | 0.73 & 4.87	60.36	60.59	0.996	0.23
C/C_TS_r0.22/r4.55_L150		4.59 & 1.01 | 1.01 & 4.59	77.41	77.64	0.997	0.23
C/C_TS_r0.25/r4.00_L150		4.48 & 1.12 | 1.12 & 4.48	83.19	83.93	0.991	0.74
C/C_TS_r0.28/r3.57_L150		4.38 & 1.22 | 1.22 & 4.38	87.60	88.69	0.988	1.09
C/C_TS_r0.31/r3.57_L150		4.28 & 1.32 | 1.32 & 4.28	90.93	91.95	0.989	1.02
C/C_TS_r0.33/r3.00_L150		4.20 & 1.40 | 1.40 & 4.20	92.66	93.05	0.996	0.39
C/C_TS_r0.40/r2.50_L150		4.00 & 1.60 | 1.60 & 4.00	91.71	92.16	0.995	0.45
C/C_TS_r0.50/r2.00_L150		3.73 & 1.87 | 1.87 & 3.73	85.55	86.64	0.987	1.09
C/C_TS_r0.60/r1.67_L150		3.50 & 2.10 | 2.10 & 3.50	80.56	80.96	0.995	0.40
C/C_TS_r0.70/r1.43_L150		3.29 & 2.31 | 2.31 & 3.29	76.29	76.06	1.003	0.23
C/C_TS_r0.90/r1.11_L150		2.95 & 2.65 | 2.65 & 2.95	69.21	69.01	1.003	0.20
C/A_TS_r0.10/r10.0_L150	180 | 70	4.46 & 1.15 | 0.21 & 5.39	37.50	37.33	1.005	0.17
C/A_TS_r0.12/r8.33_L150		4.23 & 1.32 | 0.25 & 5.35	41.51	41.60	0.998	0.09
C/A_TS_r0.15/r6.67_L150		4.04 & 1.56 | 0.31 & 5.29	47.53	47.76	0.995	0.23
C/A_TS_r0.22/r4.55_L150		3.58 & 2.02 | 0.44 & 5.16	61.13	61.62	0.992	0.49
C/A_TS_r0.25/r4.00_L150		3.41 & 2.19 | 0.50 & 5.10	66.81	67.72	0.987	0.91
C/A_TS_r0.28/r3.57_L150		3.26 & 2.35 | 0.55 & 5.05	72.89	73.59	0.991	0.70
C/A_TS_r0.31/r3.23_L150		3.12 &2.48 | 0.60 & 5.00	77.89	78.48	0.992	0.59
C/A_TS_r0.33/r3.00_L150		3.02 & 2.58 | 0.64 & 4.96	76.90	77.13	0.997	0.23
C/A_TS_r0.40/r2.50_L150		2.76 & 2.84 | 0.75 & 4.85	71.89	71.89	1.000	0.00
C/A_TS_r0.50/r2.00_L150		2.45 & 3.15 | 0.91 & 4.69	65.95	65.63	1.005	0.32
C/A_TS_r0.60/r1.67_L150		2.20 & 3.40 | 1.06 & 4.54	61.31	61.04	1.004	0.27
C/A_TS_r0.70/r1.43_L150		2.00 & 3.60 | 1.20 & 4.40	57.82	57.50	1.006	0.32
C/A_TS_r0.90/r1.11_L150		1.69 & 3.91 | 1.45 & 4.15	52.54	52.35	1.004	0.19

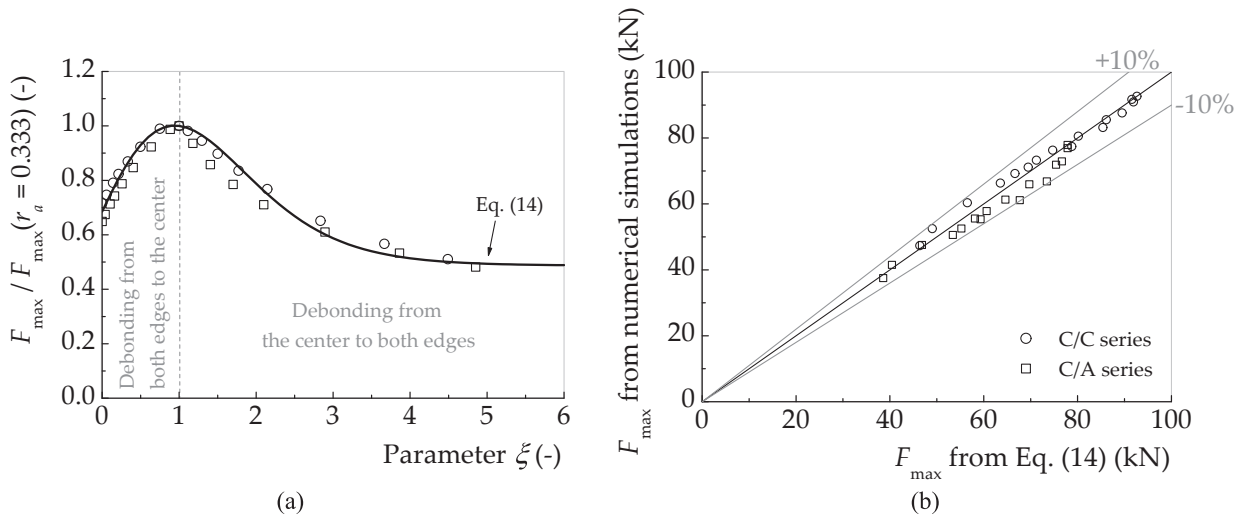

Fig. 15. Prediction of the maximum loads of different two-step bonded joints with $r_a = 1/r_b$: (a) through parameter ξ; and (b) precision of the proposed model.

joint (on the left-hand side) is assumed to have $r = 1$, i.e. as if it was treated as a one-step joint with its load capacity maximized, then we would obtain $r_a = 1/3$ and, also $r_b = 3$. To identify the values of r_a for other situations with different elastic moduli, the following equations can be used:

$$t_{a2} + t_{c1} + t_{c2} + t_{b1} - t = 0 \tag{15}$$

$$\frac{t_{b1}}{t_{a2}} \cdot \frac{t_{c1} + t_{c2} + t_{b1}}{t_{c1} + t_{c2} + t_{a2}} - \left(\frac{E_2}{E_1}\right)^2 = 0 \tag{16}$$

$$E_2 \cdot t_{a2} - E_1 \cdot t_{c1} = 0 \tag{17}$$

$$E_2 \cdot t_{c2} - E_1 \cdot t_{b1} = 0 \tag{18}$$

$$r_a = \frac{E_2}{E_1} \cdot \frac{t_{a2}}{t_{c1} + t_{c2} + t_{b1}} \tag{19}$$

where t_{c1} and t_{c2} are the thickness of materials 1 and 2 at the centre of the two-step joint, as is shown in Fig. 16. The aim of using Eqs. (15)-(19) is to calculate r_a in Eq. (19), which is achieved by assuming the following: (a) the thickness of the joint should not change (see Eq. (15)); (b) the relationship between the axial stiffness ratio of both left and right sides of the two joint is $r_a = 1/r_b$ (see Eq. (16)); and (c) the axial stiffness ratio of each step is treated like a one-step joint, in which the apparent axial stiffness ratio is equal to 1 (see Eqs. (17) and (18)).

For the C/A models where material 2 in Fig. 16 is aluminium (with $E_2 = 70$ GPa), the value obtained from this procedure indicates that the load capacity of the two-step joint is maximized when $r_a = 0.31$ and $r_b = 3.23$, which is corroborated by the results shown in Table 3. To better understand the influence of the axial stiffness ratio r_a with the elastic modulus of the adherends, this same procedure was carried out for different elastic moduli. The results are shown in Fig. 17 and they reveal that the value of r_a varies with the quotient between the elastic modulus of material 2 with the elastic modulus of material 1 (E_2/E_1). At the same time, it can be seen that only with a meaningful difference between both elastic moduli does the axial stiffness ratio r_a that leads to a maximized load capacity of the two-step joint move away from $r_a = 1/3$ and $r_b = 3$ (with $E_2 = E_1$). For instance, only with E_2/E_1 lower than 0.2 is the deviation from $E_2 = E_1$ higher than 20% and for the C/A specimens this deviation is<10% (see Fig. 17a). In Fig. 17b, the variation of the normalized thicknesses (t_i/t) is shown for the four different thicknesses defined in Fig. 16, t_{a1}, t_{b1}, t_{c1} and t_{c2}, with the variation of the elastic modulus of the adherends. Compared with the situation with $E_1 = E_2$, the thickness t_{a2} increases, while t_{c1} decreases when $E_2 < E_1$. However, t_{c2} tends to increase slightly and only begins to decrease for $E_2 \ll E_1$, while t_{b1} decreases for any situation where $E_2 < E_1$.

To confirm this analytical interpretation, fifteen more numerical specimens were considered. Table 4 shows the characteristics of these new models in which a total bonded length of 150 mm and 50 mm wide was used, as before. Moreover, the elastic modulus of material 1 was assumed to be 180 GPa in all the models and it was combined with five different materials with an elastic modulus of 18 GPa, 36 GPa, 54 GPa, 108 GPa and 144 GPa each, leading to an E_2/E_1 equal to 0.1, 0.2, 0.3, 0.6 and 0.8, respectively. The choice of these values aimed to cover a wide range of E_2/E_1 values that could cover different situations, as shown in Fig. 17. Furthermore, only three models with the same E_2/E_1 were considered, one that is expected to have the highest load capacity (relative maximum) and the other two, sufficiently close to the first one, where it is expected to have lower load capacities. It should be mentioned that one of these two cases is a similar specimen (with the same elastic modulus) to $r_a = 1/3$ and its results were considered as reference values.

With a few exceptions, the results confirm that when the two-step joint has a $r_a = 1/3$ the load capacity of the joint is maximized. The exception lies in those cases where $E_2 \ll E_1$. This may be explained by the very low thicknesses that should be adopted on the right-hand side of the joint that may not have been considered by the numerical approaches used. It should be noted also that since the specimens with $E_2 = 18$ GPa led to very small thicknesses of the CFRP composite, the rupture of the CFRP was predicted by both numerical methods. These cases would be very difficult to test experimentally since they require the manufacture of joints with thicknesses of<0.2 mm. Moreover, the differences from the case with $r_a = 1/3$ are quite marginal and it seems that the "rule of 1/3" can be recommended for the axial stiffness of the left-hand side of the two-step joint. The results obtained from both numerical methods are quite close to each other and only in two cases did the relative deviation exceed 2.0% (with a maximum of 8.0%).

7. Conclusions

In the present work, the influence of the configuration of stepped-lap joints was analysed, and two main configurations were considered: with one or two-steps. By using two different numerical implicit and explicit methods (FEM and DEM, respectively), we expected to show the feasibility of all results herein reported. Based on a total of 162 numerical simulations (i.e. 81 different simulated models per numerical method), it is possible to enumerate the following main conclusions:

1) The results obtained from the numerical modelling of the one and two-step joints with the FEM and DEM were very consistent, validating thereby, the numerical results. Only marginal deviations between both numerical methods were obtained. For instance, in only a couple of simulations, the absolute deviation between them has slightly exceeded 1.0 kN;
2) From the point of view of the bond capacities of the joints, for the same total bonded length, the use of a second step does not mean that the load capacity can always be increased. When r_a and r_b were both close to 1.00, for instance with $r_a = 0.78$ and $r_b = 1.00$ the load capacity of the two-step joint approximated the load capacity value of the one-step joint with $r_a = 1.00$. However, the load capacity of the two-step joints can be maximized by using a geometry where $r_a = 1/r_b$. The proposed semi-empiric model to estimate the load capacities of these types of two-step bonded joints (with $r_a = 1/r_b$) led to estimated values lower than 10% of those obtained numerically;

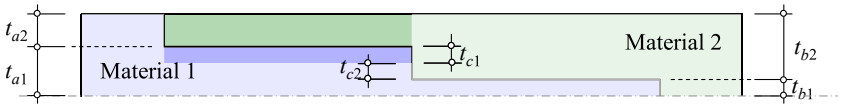

Fig. 16. Illustration showing how to obtain a two-step configuration bonded joint with a maximized load capacity.

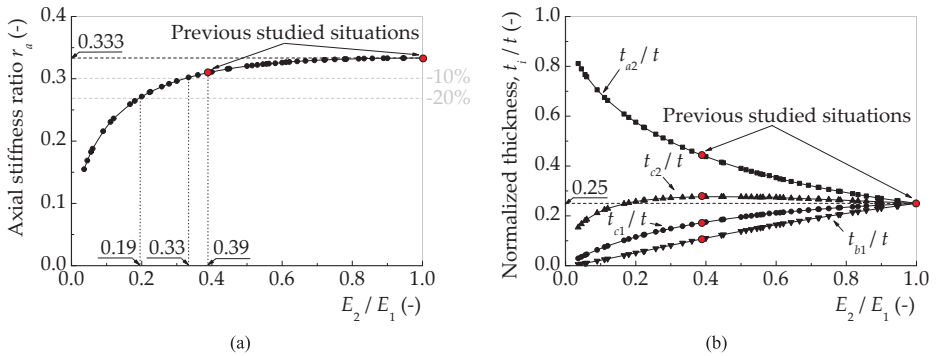

Fig. 17. Prediction of the maximum loads of different two-step bonded joints with $r_a = 1/r_b$: (a) through parameter ξ; and (b) precision of the proposed model.

Table 4
Identification of the two-step bonded joints with a maximized load capacity.

E_1 (GPa)	E_2 (GPa)	E_2/E_1	t_{a2} (mm)	t_{c1} (mm)	t_{c2} (mm)	$t_{c1}+t_{c2}$ (mm)	t_{b1} (mm)	r_a	FEM (kN)	DEM (kN)	$F_{max}^{(FEM)}/F_{max}^{(DEM)}$	Absolutedeviation (kN)
180	18	0.10	3.733	–	–	1.757	0.110	0.200	27.07[(1)]	25.96[(1)]	1.067	1.11
			3.868	0.387	1.223	1.610	0.122	0.223	27.62[(1)]	28.10[(1)]	0.983	0.48
			4.308	–	–	1.111	0.181	0.333	38.43[(1)]	38.08[(1)]	1.009	0.35
	36	0.20	3.111	–	–	2.222	0.267	0.250	55.14	55.07	1.001	0.07
			3.225	0.645	1.442	2.087	0.288	0.271	58.34	58.53	0.997	0.19
			3.500	–	–	1.750	0.350	0.333	58.27	58.27	1.000	0.00
	54	0.30	2.600	–	–	2.595	0.405	0.260	70.28	64.65	1.080	5.63
			2.783	0.835	1.524	2.359	0.457	0.296	70.66	71.31	1.009	0.65
			2.947	–	–	2.144	0.509	0.333	69.43	69.72	1.004	0.29
	108	0.60	1.908	–	–	3.384	0.878	0.310	85.21	83.01	1.026	2.20
			1.972	1.183	1.528	2.711	0.917	0.326	86.16	87.00	1.010	0.84
			2.000	–	–	2.667	0.933	0.333	85.92	87.11	1.014	1.19
	144	0.80	1.600	–	–	2.859	1.141	0.320	89.57	90.29	0.992	0.72
			1.642	1.314	1.469	2.783	1.175	0.332	89.83	90.83	0.989	1.00
			1.647	–	–	2.774	1.179	0.333	89.98	90.87	0.990	0.89

[(1)] Cohesive rupture of the CFRP composite.

3) Considering that within the interval of $0 \leq r \leq 1$, the load capacity of one-step joints increases with the increase of the axial stiffness ratio, but it will decrease if $r > 1$, the localization of the debonding initiation of a two-step joint can be identified on the side where the load capacity is expected to be lower, i.e. on the side where lower bond stresses develop. However, if the same amount of bond stress is expected to develop on both sides of the two-step joint, then the debonding initiation will occur on both sides of the joint. This is the case when the geometry of the specimens has the geometrical condition with the following axial stiffness ratio relationship of $r_a = 1/r_b$;
4) The debonding sequence can be shifted from one side to another by changing the axial stiffness ratio properly. Thus, from an original two-step joint with r_a and r_b, the new joint with an opposite debonding process can be defined by using: (i) a r_a value equal to the r_b value of the original joint; and (ii) a r_b value that is $1/r_a$ of the original joint. For instance, the debonding sequence of specimen C/C_TS_r0.19/r0.78_L150 is the same, but developed in the opposite direction as that observed in specimen C/C_TS_r0.78/r5.14_L150;
5) The load capacity of a two-step configuration can be maximized if the "rule of 1/3" is applied, i.e. if the geometry condition of $r_a = 1/3$ and $r_b = 3$ is adopted. Despite the fact this may not be observed in some cases where $E_2 \ll E_1$, the results indicated that the difference between the maximum load and the load obtained when $r_a = 1/3$ showed irrelevant differences. It should also be noted that the "rule of 1/3" may be difficult (or even impossible) to put into practice experimentally in those cases where $E_2 \ll E_1$, since it demands that the right-hand side of the joint has a thickness of<0.5 mm.

Finally, the authors recognize here that the present work would have benefited if experimental work had also been carried out. However, one main goal of this work was to make a comparison between the results obtained from two different numerical methods (FEM and DEM) and, therefore, provide feasible results that could facilitate the identification of any doubts that all analysed joint configurations could raise even before carrying out any experimental testing. So, the identification of the most favourable joints with a stepped configuration will allow us to implement them in an experimental programme in the future.

CRediT authorship contribution statement

Hugo C. Biscaia: Writing – review & editing, Writing – original draft, Validation, Supervision, Software, Resources, Project administration, Methodology, Investigation, Funding acquisition, Data curation, Conceptualization. **Rui Micaelo:** Writing – review & editing, Writing – original draft, Validation, Software, Resources, Methodology, Investigation, Data curation. **Pietro Cornetti:** Writing – review & editing, Validation. **Raquel Almeida:** Writing – review & editing, Validation, Resources.

Declaration of Competing Interest

The authors declare that they have no known competing financial interests or personal relationships that could have appeared to influence the work reported in this paper.

Data availability

Data will be made available on request.

Acknowledgments

The authors gratefully acknowledges the Foundation for Science and Technology (FCT - MCTES) for its financial support via the projects UIDB/00667/2020 and UIDP/00667/2020 (UNIDEMI), UIDB/04625/2020 (CERIS) and exploratory project JOIN4SPACE (EXPL/EME-APL/0994/2021).

References

[1] Tenney DR, Davis Jr. JG, Johnston NJ, Pipes RB, McGuire JF. (2011). Structural framework for flight: NASA's role in development of advanced composite materials for aircraft and space structures. NASA/CR-2011-217076. 504p.
[2] Gay D. (2015). Composite materials design and applications. Editions CRC Press Taylor and Francis Group, Third Edition, New York, USA, pp. 24.
[3] Haddad RH, Al-Rousan R, Almasry A. Bond-slip behavior between carbon fiber reinforced polymer sheets and heat-damaged concrete. Compos B Engng 2013;45 (1):1049–60.
[4] Silva MAG, Cidade MT, Biscaia H, Marreiros R. Composites and FRP-strengthened beams subjected to dry/wet and salt fog cycles. J Mater Civ Engng 2014;26 (12):04014092.
[5] Gong Y, Shan Y, Wu Y, Wang L, Liu X, Ding F. Bond Properties of Carbon Fiber Reinforced Polymer and Corrosion-Cracked Reinforced Concrete Interface: Experimental Test and Nonlinear Degenerate Interface Law. Materials 2021;14:5333.
[6] Nguyen TC, Bai Y, Zhao XL, Al-Mahaidi R. Durability of steel/CFRP double strap joints exposed to sea water, cyclic temperature and humidity. Compos Struct 2012;94(5):1834–45.
[7] Yang Y, Biscaia H, Silva MAG, Chastre C. Monotonic and quasi-static cyclic bond response of CFRP-to-steel joints after salt fog exposure. Compos B Engng 2019; 168:532–49.
[8] Li A, Xu S, Wang H, Zhang H, Wang Y. Bond behaviour between CFRP plates and corroded steel plates. Compos Struct 2019;220:221–35.
[9] Bodjona K, Lessard L. Hybrid bonded-fastened joints and their application in composite structures: A general review. J Reinf Plast Compos 2016;35(9):764–81.
[10] Silva MAG, Biscaia H, Ribeiro P. On factors affecting CFRP-steel bonded joints. Constr Build Mater 2019;226:360–75.
[11] Galińska A. Mechanical joining of fibre reinforced polymer composites to metals - A review. Part I: Bolted joining. Polymers 2020;12(10):2252.
[12] Fernando D, Yu T, Teng JG. Behavior of CFRP laminates bonded to a steel substrate using a ductile adhesive. J Compos Constr 2014;18(2):04013040.
[13] Li C, Ke L, He J, Chen Z, Jiao Y. Effects of mechanical properties of adhesive and CFRP on the bond behavior in CFRP-strengthened steel structures. Compos Struct 2019;211:163–74.
[14] He J, Xian G, Zhang YX. Numerical modelling of bond behaviour between steel and CFRP laminates with a ductile adhesive. Int J Adhes Adhes 2021;104: 102753.
[15] Doroudi Y, Fernando D, Nguyen VT, Torres JP. Experimental Study on CFRP-to-Steel Bonded Interfaces under Quasi-Static Cyclic Loading. J Compos Constr 2019;23(4):04019023.
[16] Al-Zubaidy H, Al-Mahaidi R, Zhao XL. Experimental investigation of bond characteristics between CFRP fabrics and steel plate joints under impact tensile loads. Compos Struct 2012;94(2):510–8.
[17] Pang Y, Wu G, Wang H, Gao D, Zhang P. Bond-slip model of the CFRP-steel interface with the CFRP delamination failure. Compos Struct 2021;256:113015.
[18] Hart-Smith LJ. (1974). Advances in the analysis and design of adhesive-bonded joints in composite aerospace structures. SAMPE Process Engineering Series, Vol. 19, SAMPE, Azusa, pp. 727-737.
[19] Troughton, MJ. Handbook of Plastics Joining: A Practical Guide. Chapter 17: Adhesive Bonding. M.J. Troughton - 2nd ed, 2008, pp. 166-173. ISBN 978-0-8155-1581-4.
[20] Banea MD, da Silva LFM. Adhesively bonded joints in composite materials: an overview. Proceed Institut Mechan Eng, Part L: J Mater Desig Appl 2009;223(1): 1–18.
[21] Space engineering Adhesive bonding handbook. ECSS-E-HB-32-21. Netherlands: ESA Requirements and Standards Division; 2011.
[22] Droubi MG, Fosbrooke C, McConnachie J, Faisal NH. Indentation based strength analysis of adhesively bonded leading-edge composite joints in wind turbine blades. SN Applied Sciences 2019;1:691.
[23] Li F, Liu Z, Duan J, Jiang F. Research on failure mode and load distribution pattern of composite pretightened tooth connections under different tooth shapes. Engng Fail Anal 2020;118:104801.
[24] Zhao B, Lu ZH, Lu YN. Closed-form solutions for elastic stress-strain analysis in unbalanced adhesive single-lap joints considering adherend deformations and bond thickness. Int J Adhes Adhes 2011;31(6):434–45.
[25] Dehghani E, Daneshjoo F, Aghakouchak AA, Khaji N. A new bond-slip model for adhesive in CFRP–steel composite systems. Engng Struct 2012;34:447–54.
[26] Biscaia HC, Chastre C. Theoretical analysis of fracture in double overlap bonded joints with FRP composites and thin steel plates. Engng Fract Mech 2018;190: 435–60.
[27] Matta F, Dawood M. Rehabilitation of Metallic Civil Infrastructure using Fiber-reinforced Polymer (FRP) Composites. Chapter 7: Rehabilitation of steel tension members using fiber-reinforced polymer (FRP) composites. Vistasp M. Karbhari ed, 2014, pp. 169-200.
[28] Shang X, Marques EAS, Machado JJM, Carbas RJC, Jiang D, da Silva LFM. Review on techniques to improve the strength of adhesive joints with composite adherends. Compos B Engng 2019;177:107363.
[29] Dobrzański P, Oleksiak W. Design and analysis methods for composite bonded joints. Trans Aerospace Res 2021;1(262):45–63.

[30] Akpinar S. The strength of the adhesively bonded step-lap joints for different step Numbers. Compos B 2014;67:170–8.
[31] Durmuş M, Akpinar S. The experimental and numerical analysis of the adhesively bonded three-step-lap joints with different step lengths. Theor Appl Fract Mech 2020;105:102427.
[32] Kanani AY, Hou X, Laidlaw R, Ye J. The effect of joint configuration on the strength and stress distributions of dissimilar adhesively bonded joints. Engng Struct 2021;226:111322.
[33] Ueda T, Dai JG. New shear bond model for FRP–concrete interface–from modeling to application. FRP Composites in Civil Engineering-CICE, Proceedings of the 2nd International Conference on FRP Composites in Civil Engineering-CICE 2004, 8–10 December 2004. Adelaide, Australia: Taylor & Francis; 2004. p. 2004.
[34] Biscaia HC, Chastre C. Design method and verification of steel plate anchorages for FRP-to-concrete bonded interfaces. Compos Struct 2018;192:52–66.
[35] Fawzia S, Zhao XL, Al-Mahaidi R. Bond-slip models for double strap joints strengthened by CFRP. Compos Struct 2010;92(9):2137–45.
[36] Wu C, Zhao X, Duan WH, Al-Mahaidi R. Bond characteristics between ultra high modulus CFRP laminates and steel. Thin-Walled Struct 2012;51:147–57.
[37] Ren FF, Yang ZJ, Chen JF, Chen WW. An analytical analysis of the full-range behaviour of grouted rockbolts based on a tri-linear bond-slip model. Constr Build Mater 2010;24(3):361–70.
[38] Zhang F, Gao L, Wei Q. Theoretical and numerical bonding capacity model of FRP-to-concrete joints with mechanical fastening. Constr Build Mater 2022;353:129066.
[39] Caggiano A, Martinelli E, Faella C. A fully-analytical approach for modelling the response of FRP plates bonded to a brittle substrate. Int J Solids Struct 2012;49(17):2291–300.
[40] Pan J, Wu YF. Analytical modeling of bond behavior between FRP plate and concrete. Compos B Engng 2014;61:17–25.
[41] Martinelli E. Closed-Form Solution Procedure for Simulating Debonding in FRP Strips Glued to a Generic Substrate Material. Fibers 2021;9:22.
[42] Benson S, Downes J, Dow RS. Ultimate strength characteristics of aluminium plates for high-speed vessels. Ships Offshore Struct 2011;6(1–2):67–80.
[43] Lazarescu L, Ciobanu I, Nicodim IP, Comsa DS, Banabic D. Effect of the mechanical parameters used as input data in the yield criteria on the accuracy of the finite element simulation of sheet metal forming processes. Key Engng Mater 2013;554–557:204–9.
[44] Bałon P, Rejman E, Smusz R, Szostak J, Kiełbasa B. (2018). Implementation of high speed machining in thin-walled aircraft integral elements Open Engineering, 8:162-169.
[45] Fernández DM, Rodríguez-Prieto A, Camacho AM. Prediction of the bilinear stress-strain curve of aluminum Alloys Using Artificial Intelligence and Big Data. Metals 2020;10(7):904.
[46] Lu XZ, Teng JG, Ye LP, Jiang JJ. Bond-slip models for FRP sheets/plates bonded to concrete. Engng Struct 2005;27(6):920–37.
[47] Biscaia H, Chastre C, Silva MAG. Estimations of the debonding process of aged joints through a new analytical method. Compos Struct 2019;211:577–95.
[48] Biscaia H. Closed-form solutions for modelling the response of adhesively bonded joints under thermal loading through exponential softening laws. Mech Mater 2020;148:103527.
[49] Guo X, Wu Z, Yang Y, Bai J, Zhou Q. A Study on the bond-slip relationship of the CFRP-steel interface of CFRP strengthened steel. Materials 2022;15:4187.
[50] Yuan H, Lu X, Hui D, Feo L. Studies on FRP-concrete interface with hardening and softening bond-slip law. Compos Struct 2012;94(12):3781–92.
[51] Wan J, Smith ST, Qiao P, Chen F. Experimental investigation on FRP-to-timber bonded interfaces. J Compos Constr 2014;18(3):A4013006.
[52] Červenka V, Jendele L, Červenka J. ATENA Program Documentation (Part 1): Theory Červenka Consulting, Prague (2016).
[53] Biscaia HC, Chastre C, Silva MAG. Modelling GFRP-to-concrete joints with interface finite elements with rupture based on the Mohr-Coulomb criterion. Constr Build Mater 2013;47:261–73.
[54] Biscaia HC, Chastre C, Silva MAG. A smeared crack analysis of reinforced concrete T-beams strengthened with GFRP composites. Engng Struct 2013;56:1346–61.
[55] Biscaia H. The influence of temperature variations on adhesively bonded structures: A non-linear theoretical perspective. Int J Non Linear Mech 2019;113:67–85.
[56] Potyondy DO, Cundall PA. A bonded-particle model for rock. Int J Mechan Min Sci 2004;41(8):1329–64.
[57] Biscaia H, Micaelo R. Emerging anchored FRP systems bonded to steel subjected to monotonic and cyclic loading: A numerical study. Engng Fract Mech 2022;261:108250.
[58] Ketterhagen WR, am Ende MT, Hancock BC. Process Modeling in the Pharmaceutical Industry using the Discrete Element Method. J Pharm Sci 2009;98(2):2009.
[59] Rojas E, Vergara V, Soto R. Case study: Discrete element modeling of wear in mining hoppers. Wear 2019;430–431:120–5.
[60] Zhang P, Lei D, Ren Q, He J, Shen H, Yang Z. Experimental and numerical investigation of debonding process of the FRP plate-concrete interface. Constr Build Mater 2020;235:117457.
[61] Biscaia H, Micaelo R, Chastre C. Cyclic performance of adhesively bonded joints using the Distinct Element Method: Damage and parametric analysis. Compos B Engng 2019;178:107468.
[62] Azevedo NM, Candeias M, Gouveia F. (2015). A rigid particle model for rock fracture following the Voronoi tessellation of the grain structure: formulation and validation. Rock Mechan Rock Eng, 48(2):535-57.
[63] Dai J, Ueda T, Sato Y. Unified Analytical Approaches for Determining Shear Bond Characteristics of FRP-Concrete Interfaces through Pullout Tests. J Adv Concr Technol 2006;4(1):133–45.
[64] Ouezdou MB, Bae WS, Belarbi A. Effective bond length of externally bonded FRP sheets. Fourth International Conference on FRP Composites in Civil Engineering (CICE2008) At: Zurich, Switzerland; July 2008.
[65] Zhou YW, Wu YF, Yun Y. Analytical modeling of the bond-slip relationship at FRP-concrete interfaces for adhesively-bonded joints. Compos B Engng 2010;41(6):423–33.
[66] Ali-Ahmad MK, Subramaniam KV, Ghosn M. Analysis of Scaling and Instability in FRP-Concrete Shear Debonding for Beam-Strengthening Applications. J Engng Mech 2007;133(1):58–65.
[67] Carrara P, Ferretti D, Freddi F, Rosati G. Shear tests of carbon fiber plates bonded to concrete with control of snap-back. Engng Fract Mech 2011;78(15):2663–78.
[68] Zou X, D'Antino T, Sneed LH. Investigation of the bond behavior of the fiber reinforced composite-concrete interface using the finite difference method (FDM). Compos Struct 2021;278:114643.